Chinese Journal of Aeronautics, (2026), 39(1): 103530

Chinese Society of Aeronautics and Astronautics
& Beihang University

Chinese Journal of Aeronautics

cja@buaa.edu.cn
www.sciencedirect.com

FULL LENGTH ARTICLE

Multi-objective topology optimization for cutout design in deployable composite thin-walled structures

Hao JIN [a], **Ning AN** [b,*], **Qilong JIA** [b,c], **Chun SHAO** [a], **Xiaofei MA** [d], **Jinxiong ZHOU** [e,*]

[a] *School of Mechanical Engineering, Hangzhou Dianzi University, Hangzhou 310018, China*
[b] *Key Laboratory of Advanced Spatial Mechanism and Intelligent Spacecraft, Ministry of Education, School of Aeronautics and Astronautics, Sichuan University, Chengdu 610065, China*
[c] *Jeatron Technology Co., Ltd., Shanghai 201800, China*
[d] *China Academy of Space Technology (Xi'an), Xi'an 710100, China*
[e] *State Key Laboratory for Strength and Vibration of Mechanical Structures and School of Aerospace, Xi'an Jiaotong University, Xi'an 710049, China*

Received 21 November 2024; revised 13 December 2024; accepted 8 March 2025
Available online 8 April 2025

KEYWORDS

Composite laminates;
Deployable structures;
Multi-objective optimization;
Thin-walled structures;
Topology optimization

Abstract Deployable Composite Thin-Walled Structures (DCTWS) are widely used in space applications due to their ability to compactly fold and self-deploy in orbit, enabled by cutouts. Cutout design is crucial for balancing structural rigidity and flexibility, ensuring material integrity during large deformations, and providing adequate load-bearing capacity and stability once deployed. Most research has focused on optimizing cutout size and shape, while topology optimization offers a broader design space. However, the anisotropic properties of woven composite laminates, complex failure criteria, and multi-performance optimization needs have limited the exploration of topology optimization in this field. This work derives the sensitivities of bending stiffness, critical buckling load, and the failure index of woven composite materials with respect to element density, and formulates both single-objective and multi-objective topology optimization models using a linear weighted aggregation approach. The developed method was integrated with the commercial finite element software ABAQUS via a Python script, allowing efficient application to cutout design in various DCTWS configurations to maximize bending stiffness and critical buckling load under material failure constraints. Optimization of a classical tubular hinge resulted in improvements of 107.7% in bending stiffness and 420.5% in critical buckling load compared to level-set topology

* Corresponding authors.
E-mail addresses: anning@scu.edu.cn (N. AN), jxzhouxx@mail.xjtu.edu.cn (J. ZHOU).
Peer review under responsibility of Editorial Committee of CJA

https://doi.org/10.1016/j.cja.2025.103530

optimization results reported in the literature, validating the effectiveness of the approach. To facilitate future research and encourage the broader adoption of topology optimization techniques in DCTWS design, the source code for this work is made publicly available via a GitHub link: https://github.com/jinhao-ok1/Topo-for-DCTWS.git.

1. Introduction

By introducing cutouts into thin-walled composite structures, a novel class of deployable structures has been created, referred to as Deployable Composite Thin-walled Structures (DCTWS), which have found a wide range of applications in aerospace engineering due to their lightweight nature, high deployment-to-stowage ratio, and self-deployment capability.[1] Examples of DCTWS applications include spaceborne antennas, solar arrays and large deployable mirrors,[2–10] as presented in Fig. 1. These structures are designed to be folded compactly during launch to minimize the use of rocket's payload space and then deployed in orbit toserve as supporting structures for large-scale space mechanisms. The cutouts in DCTWS, on the one hand, add flexibility to the structures, enabling them to be folded into a compact form without causing material failure. On the other hand, the cutouts also reduce the stiffness and load-bearing capability of the structures in their fully deployed state. This creates a trade-off between flexibility and structural integrity of the structure, necessitating a series of structural optimization problems. Engineers must carefully design and analyze these cutouts to achieve an optimal balance, ensuring that the deployable structures perform effectively in their intended aerospace applications while maintaining their durability and reliability.

The design and optimization of cutouts in DCTWS present numerous challenges. First, DCTWS are composed of anisotropic composite laminates, which require the application of complex material failure criteria. Second, their folding and deployment processes often involve highly nonlinear geometric deformations, including buckling and snap-through phenomena, indicative of structural instabilities. To accurately capture these phenomena, the finite element method (FEM) provides a reliable approach for evaluating the quasi-static folding and deployment performance of DCTWS.[11,12] However, achieving

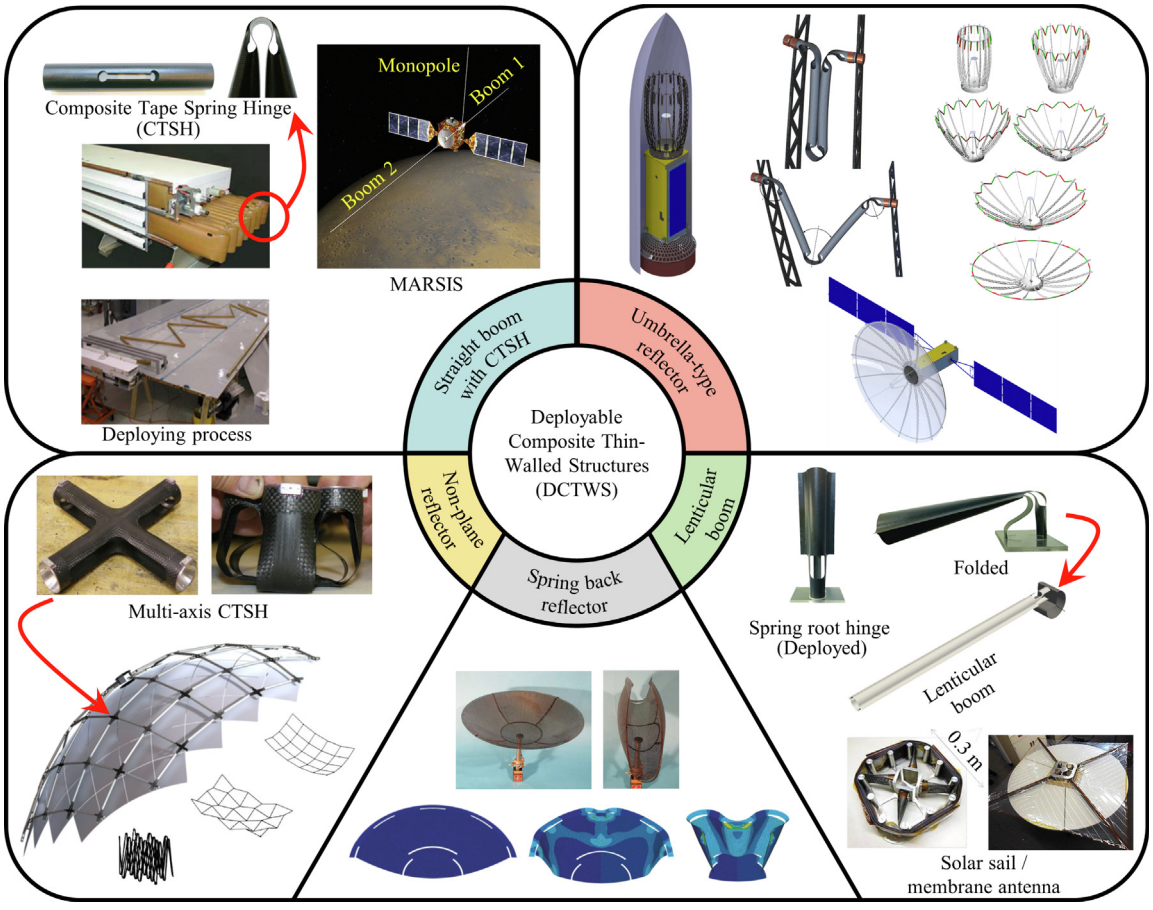

Fig. 1 Deployable Composite Thin-walled Structures (DCTWS) and their applications in space engineering.

numerical convergence and maintaining accuracy typically require significant computational time. A relatively straightforward strategy for optimizing cutout design involves parameterized modeling of the geometric contours of the cutouts, which allows the formulation of size and shape optimization problems. These problems can then be solved using optimization algorithms based on gradient information or heuristic search methods, but each has notable limitations. Gradient-based search algorithms require fewer iterations; however, they are prone to becoming trapped in local optima when addressing highly nonlinear optimization problems. In contrast, heuristic algorithms can achieve global optima but often require a large number of iterations. Coupling heuristic algorithms with high-fidelity FEM models for DCTWS leads to prohibitively high computational costs. To enhance optimization efficiency, the main-stream approach involves replacing high-fidelity FEM models with surrogate models, which are then coupled with heuristic algorithms for cutout optimization.[1,13–17] While this approach has been employed by numerous researchers to improve specific performance metrics of DCTWS, it faces challenges in addressing more complex multi-objective optimization problems, such as material failure, folding-deployment performance, load-bearing capacity, and structural stability. Increasing the number of control points or adopting higher-order spline functions may offer some improvement. However, in multi-cutout collaborative designs, issues such as control point interference, spline curve intersection, and the substantial increase in design variables can significantly degrade the surrogate model's fitting accuracy. Consequently, the current state of DCTWS cutout optimization remains largely reliant on design experience or engineering intuition for improving initial designs.

Topology optimization is a more advanced and complex method compared to size and shape optimization. Theoretically, it can be divided into two main categories: material-based models and boundary-based models.[18] Material-based models include the Solid Isotropic Material with Penalization (SIMP) method, Evolutionary Structural Optimization (ESO), Bi-directional Evolutionary Structural Optimization (BESO), and Independent Continuous Mapping (ICM).[19–21] On the other hand, boundary-based models encompass the Level-set method,[22] moving deformable components method[23] among others. Material-based topology optimization typically refers to density-based approaches, where the density of each finite element serves as a design variable. Starting from the finite element equilibrium equations, the relationship between the optimization objective and the design variables is derived, followed by sensitivity expressions of each design variable concerning the optimization objectives or constraints. In each iteration, inefficient elements (forming cutouts or holes) are gradually removed based on their contribution to the objective function until constraints and convergence criteria are met, resulting in an optimal material distribution scheme. In contrast, boundary-based topology optimization fundamentally involves reshaping the material distribution by constructing explicit or implicit high-dimensional functions to describe the local sensitivity to the objective function. The boundaries of cutouts are depicted using contour lines or isosurfaces, with the Level-set method currently being the most widely applied. This optimization process considers the number, shape, and size of voids, as well as the continuity of the structure, effectively reshaping the material distribution. This concept perfectly fits the notch design problem of DCTWS, offering significant potential for expanding the design space.

In recent years, many scholars have extended classical models and successfully applied them to the optimization of composite laminated structures. Broadly, these studies fall into two categories: constant-stiffness design and variable-stiffness design.[24,25] In constant-stiffness design, laminate layers are uniform and consistent across the structure. Optimization is typically achieved through search algorithms (e.g., gradient-based methods or heuristic algorithms) to determine optimal parameters such as layer count, orientation, and thickness, or via topology optimization to reshape material distribution for structural efficiency. A notable advancement in this field is the parallel optimization framework proposed by Zhou et al.,[26] which integrates topology optimization and search algorithms to enable simultaneous optimization of laminate layup and structural topology in braided composite laminates. Variable-stiffness design, on the other hand, introduces greater complexity by allowing laminates to be discretized into regions with distinct layup designs or modeled as a continuous system where fiber angles vary spatially across the structure. While search algorithms remain effective for the former, the latter poses significant computational challenges due to fiber continuity constraints, often resulting in prohibitively high optimization costs. To address these challenges, topology optimization has demonstrated significant advantages by enabling the concurrent optimization of material distribution and local fiber orientation. Early methods, based on homogenization theory, focused on determining structural topology and using principal stress directions within elements to define local fiber orientations.[27] Building on this foundation, Lund et al. established explicit relationships between laminate parameters-such as layer count, fiber orientation, and relative density-and the stiffness matrix of discrete elements.[28] They further introduced the Discrete Material Optimization (DMO) method, which achieves globally optimal fiber paths and has become a cornerstone for advancing variable-stiffness laminate topology optimization.[29,30] Recent developments in numerical techniques have led to high-precision multiscale finite element methods that iteratively perform homogenization and de-homogenization. These methods have facilitated the integrated design of micro-structures and macro-structures, significantly enhancing variable-stiffness laminate optimization.[31–33] Nevertheless, practical applications still face major manufacturing challenges, including defects, layer overlap, and maintaining the continuity of curved fibers. These limitations highlight the need for further innovations to fully realize the potential of variable-stiffness laminate designs.

Notably, the topology optimization of composite laminated thin-walled structures primarily focuses on compliance design for small-deformation elastic structures, where the creation of cutouts or voids aims to balance structural rigidity and lightweight design. In contrast, the cutout design for DCTWS targets damage-free folding (involving large geometric deformations) and enhanced load-bearing capacity and stability after deployment. This unique requirement introduces a complex trade-off between rigidity and flexibility, highlighting both the innovation and challenges of the topology optimization research presented in this study. Additionally, DCTWS consistently emphasizes four key mechanical properties: material failure, strain energy storage, structural stiffness, and buckling

stability. While the optimization of strain energy storage and structural stiffness can be equivalently addressed using classical compliance-based topology optimization models, the optimization of material failure and buckling stability remains challenging, particularly in the derivation of sensitivity equations. These factors constrain the applicability of existing topology optimization theories to DCTWS.

In isotropic materials, topology optimization commonly employs the P-norm function to aggregate the von Mises stresses of discrete elements into a continuous function. By differentiating, sensitivity expressions of the stress objectives or constraint functions are obtained to guide structural optimization, eliminating stress concentration phenomena and striving for as uniform a stress field distribution as possible. This effectively prevents local failures and limits the ultimate strength of structures under specific deformations, a method validated by extensive research. However, the complex failure behaviors of composite materials cannot be directly described using a single von Mises stress. Instead, a variety of customized failure criteria are required, typically expressed as complex polynomials, which hinder the sensitivity analysis in topology optimization. Lee et al. improved the classical laminated plate theory by deriving the static finite element equilibrium equations for composite laminated plates considering interlaminar transverse shear deformation.[34] Building on this, and leveraging the aforementioned classical stress-based topology optimization concepts, they derived sensitivity expressions for the Tsai-Hill and Tsai-Wu criteria and used the SIMP topology optimization algorithm to solve for the optimal topology and layup angles of composite laminated plates, effectively reducing the concentration of failure indices. Recently, Zhang et al. employed a similar approach within the BESO framework to achieve stiffness topology optimization of composite laminated plates under Tsai-Wu failure criterion constraints, maximizing stiffness while ensuring structural integrity.[35] These two studies provide significant support for the development of topology optimization with composite material failure constraints. However, their research primarily focuses on the statics of two-dimensional planar structures, and their adaptability to three-dimensional shell element optimization problems, similar to those in DCTWS, remains to be further explored. Another challenge is the establishment of buckling stability topology optimization models. Buckling issues frequently arise under load conditions after DCTWS has been deployed and locked in orbit, such as in large solar sails' composite thin-walled pods or the weak edges of deployable hinge cutouts.[2,36] Common buckling topology optimization models are typically based on linear eigenvalue analysis finite element theory, aiming to maximize the critical buckling load of a structure under a specified volume. However, pseudo-modes or local buckling modes present major challenges in buckling topology optimization. Pseudo-modes tend to occur in low-density element regions during the structural topology evolution process, while local buckling modes are prevalent in slender structures commonly found in low-volume fraction structures. The occurrence of either numerical issue can lead to the failure of buckling topology optimization. Numerous scholars have developed material interpolation schemes tailored to different topology optimization theoretical frameworks, reducing stress singularity levels during the optimization process to suppress these issues.[19,37–39] These approaches have achieved good results in buckling topology optimization of two-dimensional planar structures, but these studies have yet to address three-dimensional thin-shell structures.

In summary, topology optimization is significantly beneficial for enhancing the deployment capabilities and in-orbit service performance of DCTWS, yet it still faces numerous challenges. To date, only Ferraro and Pellegrino[40] have conducted related research. They employed specific high-dimensional level-set functions, adjusting function parameters to generate isosurfaces of various shapes. By projecting these isosurfaces onto the high-strain regions of the Right Angle Woven Composite Tubular Hinge (RA-WCTH), they created cutouts of different quantities and shapes. Subsequently, different notch schemes were subjected to finite element simulations to verify structural integrity and bending stiffness, thereby selecting the optimal results. This study is unrelated to level-set topology optimization theory and represents a single-objective optimization problem without sensitivity analysis. However, the multi-notch schemes with continuous boundaries obtained proved superior to single-notch shape optimization designs, validating the potential value of exploring topology optimization methods suitable for DCTWS.[41] Additionally, it provides a benchmark for evaluating the effectiveness of new methods.

Unlike Ferraro's single-objective optimization problem,[40] this paper formulates a multi-objective optimization problem constrained by plain-weave composite material failure criteria. The goals are to maximize the bending stiffness, critical buckling load, and stored strain energy of DCTWS. Solving this optimization problem ensures structural integrity during the folding process while maximizing strain energy storage and providing excellent stability and deformation resistance upon deployment. It is important to clarify that this study uses the classical topology optimization concept of overall stiffness (or compliance) to approximate bending stiffness. Under displacement-based boundary conditions, higher bending stiffness results in greater strain energy generated by deformation, thereby significantly enhancing the self-deploying capability of DCTWS. Therefore, in this study, bending stiffness and stored strain energy are treated as equivalent optimization objectives. Unlike isotropic materials, which are described by a single Young's modulus, the anisotropic behavior of composite laminated plates is characterized by the ABD stiffness matrix. However, classical laminated plate theory exhibits significant errors in predicting the constitutive behavior of woven composite laminated plates,[42] complicating the accurate acquisition of response functions for DCTWS's objective or constraint functions. To address this issue, this study adopts a micro-meso multi-scale homogenized finite element analysis framework based on the Kirchhoff plate assumption to accurately obtain the ABD matrices of woven composite laminated shell elements. Building on this, within the BESO theoretical framework,[43] sensitivity expressions for compliance, critical buckling load, and customized Tsai-Wu failure criteria[44] were derived. The sensitivity derivation of the failure assessment function utilizes the stress-based topology optimization concept with the P-norm function. Notably, this study derived a sensitivity expression for critical buckling load described by unit strain energy, avoiding the cumbersome handling of stress and stiffness matrices. Its stability and effectiveness have been validated by Munk et al.[45] Additionally, because the notch optimization area in this study is relatively small compared

to the entire structure, no local buckling modes occurred during the optimization process. Therefore, numerical singularity issues in buckling topology optimization are beyond the scope of this paper. By linearly superimposing the normalized functions of each objective or constraint, a multi-objective topology optimization model was developed. Compared to Ferraro's research,[40] this paper formally proposes a sensitivity analysis-based topology optimization method to address the notch design problem of DCTWS. This model is integrated with ABAQUS through Python scripts, enabling efficient application to various DCTWS structures. Using RA-WCTH topology optimization case from Ferraro as a benchmark,[40] the optimized designs and experimental results validate the effectiveness and advantages of the proposed method.

The remaining content of the paper is structured as follows: Section 2 describes the multi-scale finite element modeling of RA-WCTH, focusing on its folding, unfolding, and critical buckling behavior. This section also explores classical cutout designs derived from engineering intuition and analyzes how variations in dimensional parameters and shape influence the performance of RA-WCTH, thereby highlighting the need for topology optimization. Section 3 presents a detailed mathematical formulation of the multi-objective topology optimization problem, along with the establishment and implementation of the optimization framework. Section 4 discusses the optimization results. Finally, Section 5 concludes the paper.

2. Mechanical behavior of RA-WCTH

2.1. Design of RA-WCTH

Fig. 2(a) illustrates the initial design of RA-WCTH which was created by Ferraro et al.[40,46] This structure consists of two thin-walled cylindrical shells connected at 90°, with a smooth transition at the junction incorporating non-zero Gaussian curvature. Each cylindrical shell has a diameter of 32 mm and extends 200 mm from the end to the intersection. The entire structure is mirror-symmetrical across both the *X*-*Y* and *Y*-*Z* planes. The RA-WCTH was fabricated using 525 Astroquartz® II plain weave fabric (quartz fiber) and a PMT-F6 cyanate ester resin matrix. This selection was based on folding tests that demonstrated a higher ultimate strain compared to epoxy resin-based carbon fiber composites. Folding tests conducted on two uniform layup schemes of RA-WCTH $[45]_2$ and [45/0/45] revealed that the double-layer design could safely fold to angles exceeding 50°, whereas the triple-layer design developed cracks upon folding to 17°, despite its higher bending stiffness. To reconcile these findings, extensive additional testing was performed, ultimately leading to the adoption of the hybrid layup scheme illustrated in Fig. 2 (b). In this scheme, high-strain concentration areas utilize the most flexible $[45]_2$ design, low-strain areas employ the thickest $[45/45/0]_s$) laminate, and transitional areas sequentially adopt the [45/0/45] and $[45]_4$ design schemes. This configuration ensures that the structure achieves maximum folding angles without requiring notch design while maintaining the highest bending stiffness in the deployed state. Here, 0° denotes the direction parallel to the RA-WCTH circular tube axis. Table 1 gives the mechanical properties of the Astroquarzt® fiber and PMT-F6 resin.[47]

2.2. Two-Scale model of woven composites

The ABD matrix is a fundamental concept in classical laminate theory (CLT), which establishes the relationship between in-plane strain, out-of-plane curvature, and the resultant internal forces and moments in the laminate. It characterizes the elastic behavior of the laminate under tensile, compressive, bending, and torsional deformations, serving as the primary approach for describing the constitutive relationships of composite shell elements. The specific form is as follows:

$$\begin{bmatrix} N_x \\ N_y \\ N_{xy} \\ M_x \\ M_y \\ M_{xy} \end{bmatrix} = \begin{bmatrix} A_{11} & A_{12} & A_{16} & B_{11} & B_{12} & B_{16} \\ A_{12} & A_{22} & A_{26} & B_{12} & B_{22} & B_{26} \\ A_{16} & A_{26} & A_{66} & B_{16} & B_{26} & B_{66} \\ B_{11} & B_{12} & B_{16} & D_{11} & D_{12} & D_{16} \\ B_{12} & B_{22} & B_{26} & D_{12} & D_{22} & D_{26} \\ B_{16} & B_{26} & B_{66} & D_{16} & D_{26} & D_{66} \end{bmatrix} \cdot \begin{bmatrix} \varepsilon_x \\ \varepsilon_y \\ \gamma_{xy} \\ \kappa_x \\ \kappa_y \\ \kappa_{xy} \end{bmatrix} \quad (1)$$

where the sub-matrix $\boldsymbol{A}$ represents the in-plane extensional stiffness properties, $\boldsymbol{D}$ represents the out-of-plane bending stiffness properties of the laminate, and $\boldsymbol{B}$ represents the coupling between in-plane and out-of-plane loads and deformations. The strains $(\varepsilon_x, \varepsilon_y, \gamma_{xy})$ and curvatures $(\kappa_x, \kappa_y, \kappa_{xy})$ correspond to the in-plane strain and out-of-plane curvature of the midplane of the laminate, respectively. The resultant forces (N_x, N_y, N_{xy}) and moments (M_x, M_y, M_{xy}) represent the internal forces and moments on the cross-section of the laminate, respectively.

Due to the complex microstructure of woven composites, the ABD matrix calculated using the CLT analytical model shows significant errors, particularly in terms of bending stiffness.[42] Therefore, before establishing the macroscale finite element model for RA-WCTH, a two-scale numerical model was developed, ranging from microscale to mesoscale, to accurately determine the ABD matrix of the woven composite laminate, as shown in the left panel of Fig. 2(b). The process begins with the development of a microscale representative volume element (RVE) comprising both yarns and resin components, using our custom plugin Viscoelastic RVE Calculator.[48] Periodic boundary conditions are applied, followed by deformations in different directions to obtain the homogenized mechanical properties of the yarns, as presented in Table 2. Subsequently, a mesoscale RVE model is constructed based on the internal geometry of the woven composite, generated using the open-source software Texgen. This model is then imported into ABAQUS, where our custom AMWC plugin automatically performs homogenization based on the Kirchhoff plate assumption, ultimately yielding the ABD matrix for the equivalent shell element.[49] Both custom plugins have been published in previous literature,[48,49] with code download links provided. The model is then imported into ABAQUS, where our custom AMWC plugin automatically performs homogenization based on the Kirchhoff plate assumption, ultimately generating the ABD matrix for the laminated plate with the specified weave pattern. The dual-scale homogenization procedure only needs to be run once before the formal topology optimization begins, with the computation typically taking less than one hour. Table 3 presents the computed ABD matrices for the different ply configurations in various regions of the RA-WCTH.

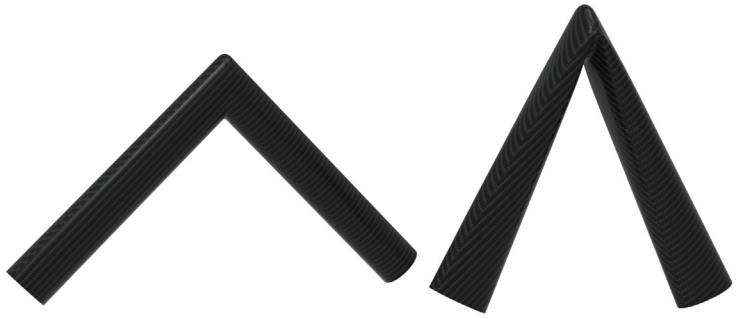

(a) Deployment and folded states of the initial RA-WCTH design

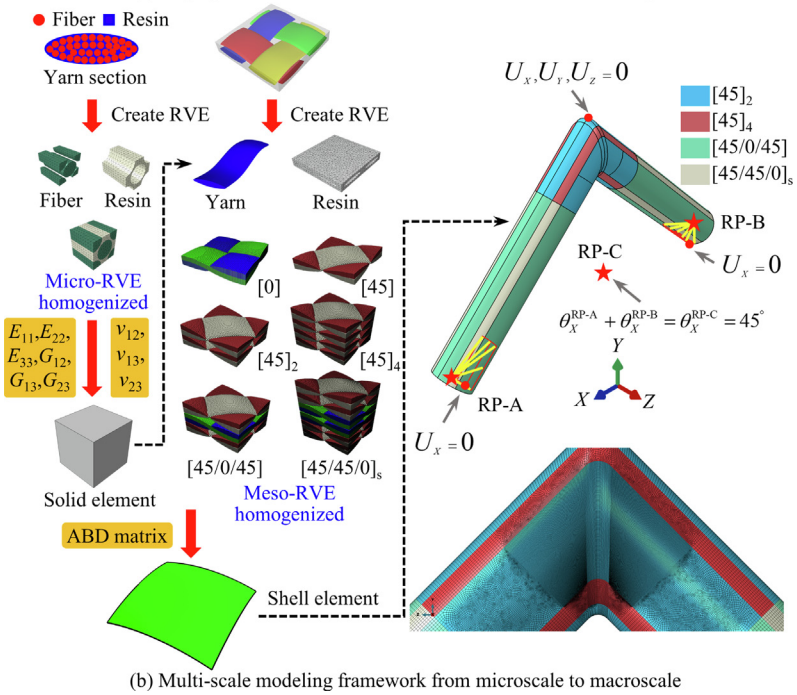

(b) Multi-scale modeling framework from microscale to macroscale

Fig. 2 Multi-scale modeling process of RA-WCTH.

Table 1 Properties of fiber and resin.[47]

Part	E (MPa)	ν	G (MPa)	d_f (μm)	V (%)
Fiber	72 000.0	0.161	31 000.0	9.0	62.0
Resin	3 640.0	0.352	1 350.0	–	38.0

Table 2 Elastic engineering constants of the composite yarns.

E_1 (MPa)	E_2 (MPa)	E_3 (MPa)	ν_{12}	ν_{13}	ν_{23}	G_{12} (MPa)	G_{13} (MPa)	G_{23} (MPa)
46 062.1	13 372.9	13 372.9	0.221	0.221	0.380	4 929.2	4 929.2	4 819.8

2.3. Macro-scale model of RA-WCTH

The macroscale finite element model of RA-WCTH was established in ABAQUS 2023 using continue shell elements (reduced integral form, S4R), with the ABD matrices from Table 3 assigned regionally according to the layup design scheme. To accurately capture deformation while optimizing computational efficiency, local mesh refinement was performed, and a mesh independence test was conducted. As a result, a total of 180 448 elements were generated, with an average mesh size of 0.125 mm in the central region and 0.7 mm in the side regions. The in-plane rotation (θ_X) of the left and right sections (highlighted by red borders) is coupled to reference points RP-A and RP-B, respectively. RP-A and RP-B are further correlated through another reference point, RP-C, following the equation ($\theta_X^{RP-A} + \theta_X^{RP-B} = \theta_X^{RP-C}$). To

Table 3 ABD Matrix for woven composite at different regions of RA-WCTH.

Laminate	A_{11} (N/mm)	A_{12} (N/mm)	A_{22} (N/mm)	A_{66} (N/mm)	D_{11} (N·mm)	D_{12} (N·mm)	D_{22} (N·mm)	D_{66} (N·mm)
$[45]_2$	3 477.1	1 923.1	3 477.1	2 118.0	3.1	1.7	3.1	1.9
[45/0/45]	5 640.9	2 121.9	5 640.9	2 402.1	10.0	5.3	10.0	5.9
$[45]_4$	6 085.0	3 365.4	6 085.0	3 706.5	23.0	12.7	23.0	14.0
$[45/45/0]_s$	9 565.1	3 598.0	9 565.1	4 073.1	69.8	37.1	69.8	40.9

induce a folding condition, θ_X^{RP-C} is gradually increased from 0° to 45°. This boundary condition ensures that the folding angles at both ends of the structure are equal. Additionally, to prevent possible rigid body movement, two nodes at the bottom of RA-WCTH (highlighted in red) are constrained to remain in the *Y-Z* plane, and the three translational degrees of freedom of the top node are fixed. The ABD matrices in Table 3 are used to simulate the material behavior of the shell elements in each layup region. The folding behavior of RA-WCTH is simulated using the Dynamic/Implicit solver in ABAQUS. Quasi-static conditions are ensured by monitoring the kinetic energy, keeping it as a small percentage of the strain energy. Linear buckling analysis of RA-WCTH was conducted using the Subspace Iteration Eigenvalue Extraction Method within the ABAQUS standard buckling analysis step, extracting the first ten eigenvalues and corresponding buckling modes. The Subspace solver was configured with 18 vectors per iteration step and a maximum of 30 iterations. During the buckling analysis, the coupling equations between the three reference points in the finite element model depicted in Fig. 2 (b) were removed, all degrees of freedom at RP-B were constrained, and a unit moment about the x-axis was applied at RP-A. This moment caused RA-WCTH to rotate and fold in the direction illustrated in Fig. 2(a).

2.4. Failure criterion for woven composites

The failure assessment of composite laminates is a complex and challenging research topic that has consistently attracted significant interest. The diversity of materials, interface behaviors, and loading forms makes it difficult to accurately evaluate failure across different scenarios using a single criterion. Therefore, the failure criterion derived by Mallikarachchi and Pellegrino,[44] based on a modified Tsai-Wu theory specifically tailored for plain-woven composite laminates, was employed. This criterion has demonstrated sufficient accuracy in the failure tests of plain-woven laminates with varying base materials and layup configurations, and it has successfully captured local failure behavior during the large deformation of multiple DCTWS structures.[11,46] The criterion defines three failure indices based on six force and moment resultants:$N_x, N_y, N_{xy}, M_x, M_y$ and M_{xy}. These indices correspond to in-plane extension(FI_1), out-of-plane bending(FI_2), and coupled in-plane extension and out-of-plane bending failure modes(FI_3), represented by the following set of inequalities:

$$\begin{cases} \mathrm{FI}_1 = f_1\left(N_x + N_y\right) + f_{11}\left(N_x^2 + N_y^2\right) + f_{12}N_xN_y + f_{33}N_{xy}^2 < 1 \\ \mathrm{FI}_2 = f_{44} \times \max\left(M_x^2, M_y^2\right) + f_{66}M_{xy}^2 < 1 \\ \mathrm{FI}_3 = \max\left(\frac{N_x}{F_x}, \frac{N_y}{F_y}\right) + \frac{\max\left(|M_x|, |M_y|\right)}{F_4} < 1 \end{cases} \tag{2}$$

The failure coefficients f_i and f_{ij} are given by the following equations:

$$\begin{cases} f_1 = f_2 = \frac{1}{F_{1t}} - \frac{1}{F_{1c}}, \quad f_{11} = f_{22} = \frac{1}{F_{1t}F_{1c}}, \quad f_{12} = -\frac{f_{11}}{2} \\ f_{33} = \frac{1}{F_3^2}, \quad f_{44} = f_{55} = \frac{1}{F_4^2}, \quad f_{66} = \frac{1}{F_6^2} \end{cases} \tag{3}$$

and

$$\begin{cases} F_x = \frac{-\left(f_1 + f_{12}N_y\right) \pm \sqrt{\left(f_1 + f_{12}N_y\right)^2 - 4f_{11}\left(f_1N_y + f_{11}N_y^2 + f_{33}N_{xy}^2 - 1\right)}}{2f_{11}} \\ F_y = \frac{-\left(f_1 + f_{12}N_x\right) \pm \sqrt{\left(f_1 + f_{12}N_x\right)^2 - 4f_{11}\left(f_1N_x + f_{11}N_x^2 + f_{33}N_{xy}^2 - 1\right)}}{2f_{11}} \end{cases} \tag{4}$$

where F_i represents the experimentally measured strength of the laminate in the direction of the yarn, with subscripts t and c denoting tension and compression, respectively. Given the use of the same woven composite material, the strength parameters reported in literature[40] were adopted, as shown in Table 4.

2.5. Mechanical mechanism of RA-WCTH

To illustrate the necessity of optimizing cutout designs, the folding behavior of the RA-WCTH without any cutouts is first examined. Fig. 3(a) depicts the evolution of the reaction bending moment as a function of the folding angle for the initial RA-WCTH design (without cutouts). As the folding angle increases, the bending moment rises, initially at a rapid rate and then slows down as the angle continues to increase. The bending stiffness, K_b, is determined by calculating the slope of the moment–angle curve in the nearly linear region near the initial point. The enclosed area under the moment–angle curve (shaded in grey) is referred to as the elastic strain energy E_b stored within the RA-WCTH when folded to 45°. Moreover, the critical buckling load of the RA-WCTH is indicated by the black dashed line, computed from linear buckling analysis. Fig. 3(b) shows the evolution of the maximum value of the three failure indices of all elements during the folding process, denoted as FI^{max}, which is plotted as a function of the folding angle. The results indicate that as the folding angle increases from 0° to 45°, FI^{max} increases quickly and exceeds

Table 4 Strength parameters for two-ply laminates.[47]

Parameter	F_{1t}, F_{2t}	F_{1c}, F_{2c}	F_3	F_4, F_5	F_6
Value (N/mm)	76.2	34.5	14.6	3.3	1.1

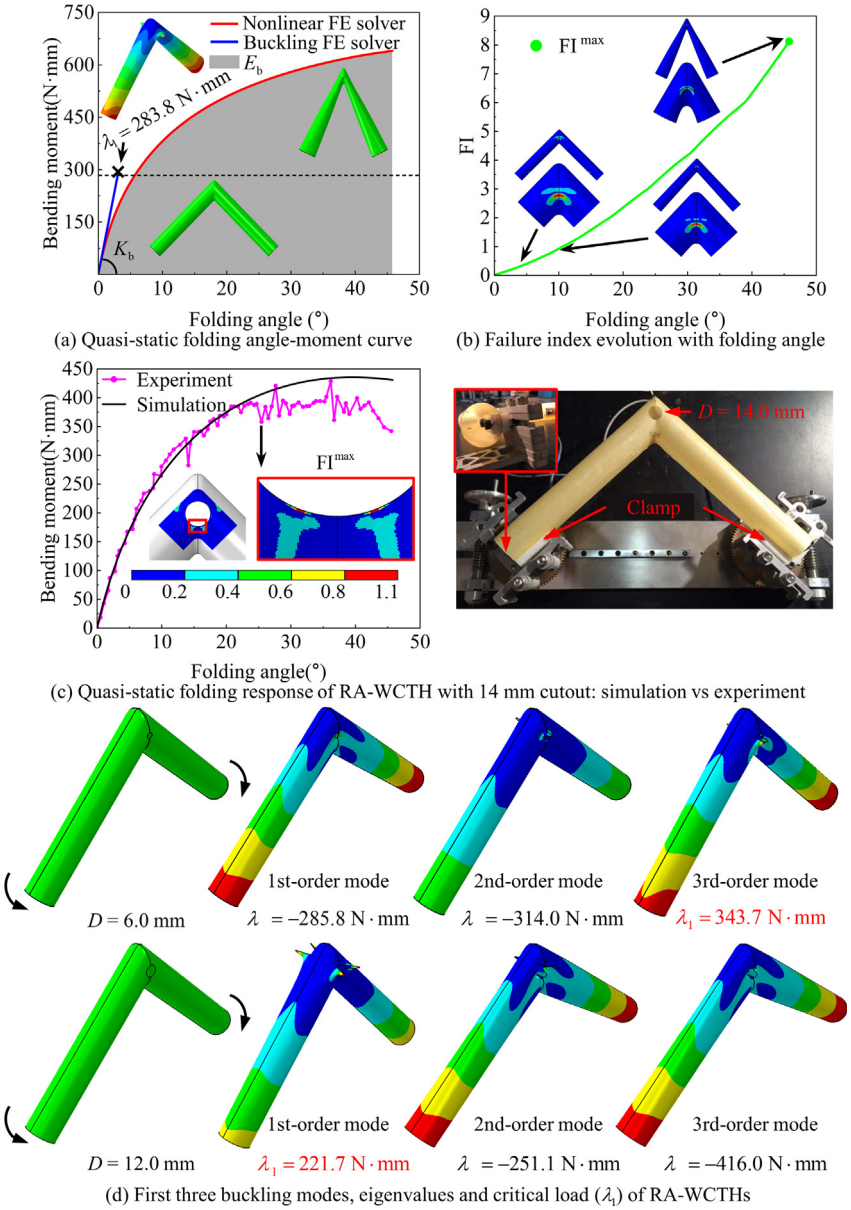

Fig. 3 Mechanical response and failure behavior of RA-WCTH.

the safety threshold at only 10°, implying a very high risk of failure for the initial RA-WCTH design. It is noted that in the folding analysis of the RA-WCTH, FI_2 and FI_3 are significantly less than the safety threshold of 1. Therefore, in the subsequent mechanical analysis, only the first expression in Eq. (2) is considered as the failure criterion, meaning that FI^{max} is equal to FI_1^{max}.

Before conducting sensitivity analysis and optimization studies on the mechanical performance response of RA-WCTH with respect to cutout design, it is crucial to first verify the accuracy of the numerical model. The experimental setup, depicted in the right image of Fig. 3(c), consists of two custom clamps that grip small regions at the ends of the two cylindrical tubes of the RA-WCTH, allowing the end cross-sections of the

tubes to deform freely. These clamps connect the tubes to rotating brackets, which are initially set at a 45° to facilitate the installation and fixation of the tube joint. During the experiment, the rotation angle is controlled by a motor, while one of the brackets is mounted on ball bearings, allowing it to slide freely towards the other fixed bracket. This arrangement enables both rotation and folding to occur simultaneously. Once the experiment begins, strain gauges and a data acquisition system are used to record the reaction moment of the RA-WCTH at various folding angles in real time. Further details about the experimental setup can be found in literature.[7] Using this platform, a quasi-static folding experiment was conducted on an RA-WCTH with a circular cutout. Fig. 3(c) compares the experimental data with the results from the numerical model, showing the angle-moment relationship. Up to a folding angle of 25°, the numerical results closely match the experimental curve. However, after 25°, a noticeable deviation occurs. Experimental observations reveal that beyond 25°, small cracks begin to form and propagate along the edges of the cutout.[7] The failure and finite element models in this study successfully capture the initiation of damage at this folding angle. However, the model does not account for the deletion of elements when the failure index exceeds a certain threshold to simulate crack propagation. As a result, the abrupt drop in load-bearing strength observed in the experimental curve is not captured by the model. This discrepancy explains the significant difference between the model and experimental results after 25°.

It is important to note this study is focused solely on the initiation of damage in the woven composite material as the failure criterion, without considering subsequent progressive damage effects. Therefore, the simulation accuracy demonstrated in Fig. 3(c) is sufficient to support the performance analysis and numerical optimization of RA-WCTH. Additionally, in linear buckling analysis, negative eigenvalues often appear to simulate buckling modes induced by loads applied in the opposite direction. However, this study concentrates exclusively on the critical buckling load that induces inward folding of the RA-WCTH. Thus, the critical buckling load referred to in this paper corresponds to the first non-negative eigenvalueλ_1, which is highlighted in red in Fig. 3(d).

According to engineering practice, mitigating material failure risk involves introducing cutouts into areas of concentrated deformation. Fig. 4 illustrates the performance of various cutout designs based on engineering intuition. Seven cases are examined, including three circular cutout designs (with radii of 4, 6, 8 mm for Cases 1, 2, and 3, respectively), and three designs with dog-bone, elliptical, and rectangular cutouts (Cases 4, 5, and 6). Case 7 represents the initial design without any cutouts for comparison. The structural performance metrics for all seven cases are compared. The results reveal that while increasing the radius of circular cutouts (Cases 1, 2, and 3) reduces the risk of failure during folding, it also significantly decreases strain energy, bending stiffness, and critical buckling load. In contrast, Cases 4, 5, and 6, which feature dog-bone, elliptical, and rectangular cutouts, respectively, all reduced the maximum failure index to below the safety threshold of 1. Notably, the elliptical cutout in Case 5, despite having the same mass as Case 4, demonstrated superior bending stiffness and buckling stability with a lower failure index. On the other hand, the rectangular cutout in Case 6, which removes material from the central region, resulted in the poorest bending stiffness and strain energy but significantly increased the buckling load.

Further analysis of Fig. 4 revealed the following: 1) Introducing simple-shaped cutouts does not eliminate the concentration of failure indices in the RA-WCTH, rather, it shifts them to the edges of the new cutouts; 2) The failure index is negatively correlated with bending stiffness, critical buckling load, and stored strain energy; 3) Bending stiffness is positively correlated with stored strain energy. Overall, the failure index, stored strain energy, and critical buckling load are highly sensitive to the size and shape of the cutout, and the interactions among them can be complex and highly nonlinear. Therefore, a rigorous mathematical formulation of the optimization problem is necessary. Advanced topology optimization methods should be employed to optimize the cutouts in the RA-WCTH, by maximizing the bending stiffness and critical buckling load while preventing material failure.

3. Optimization problem and optimization method

3.1. Topology optimization problem of RA-WCTH

The BESO method determines the optimal topology of the structure based on the relative ranking of the sensitivity magnitudes of the elements in the finite element model, allowing for the simultaneous removal and addition of material. In the BESO model, the design domain is discretized into N elements, each assigned an independent design variable x_e(e denotes the element number, with $e = 1,2, \ldots, N$), which is constrained to values of 0 or 1, where 0 represents the removal of the element and 1 represents the retention of the element. Consequently, the stiffness of each element is directly linked to the topology optimization design variable, and the element stiffness, based on the BESO material interpolation model and the ABD matrix (Eq. (5)) is expressed as:

$$\boldsymbol{D}_e = x_e \boldsymbol{D}_e^0 \tag{5}$$

where $\boldsymbol{D}_e$ is the stiffness matrix(ABD) of the e-th element material, and $\boldsymbol{D}_e^0$ represents the stiffness matrix of the element in its initial (solid) state.

Thus, the multi-objective topology optimization problem for finding the optimal shape, number, and position of cutouts to optimize the bending stiffness and critical buckling load of the RA-WCTH, while satisfying the structural material failure constraints, is defined as follows:

$$\begin{aligned} \text{Maximize}: \quad & T(X) = w_1 \cdot \bar{K}_\text{b}(X) + w_2 \cdot \bar{\lambda}_1(X) \\ & -w_3 \cdot \bar{\text{FI}}^{\max}(X) \\ \text{Subject to}: \quad & X = \{x_e\}, x_e = 0 \text{ or } 1, \forall e = 1,\ 2,\ \ldots,\ N \\ & KU = F \quad (K + \lambda_1 \boldsymbol{K}_\sigma)\boldsymbol{U}_1 = 0 \\ & \text{FI}^{\max}(X) < 1 \\ & \textstyle\sum_{i=1}^{3} w_i = 1 \end{aligned} \tag{6}$$

Through the weighted function method, the multi-objective optimization problem, which includes three independent objective or constraint functions $K_\text{b}(\boldsymbol{X})$, $\lambda_1(\boldsymbol{X})$ and $\text{FI}^{\max}(\boldsymbol{X})$, is transformed into a single-objective optimization problem $T(\boldsymbol{X})$, which is an effective and common approach.[50] $\bar{\cdot}$ represents the result of the normalization process, for example: $(K_\text{b}(\boldsymbol{X}) - K_\text{b}^{\text{opt}}(\boldsymbol{X}))/(K_\text{b}^{\text{int}}(\boldsymbol{X}) - K_\text{b}^{\text{opt}}(\boldsymbol{X}))$, where the superscript

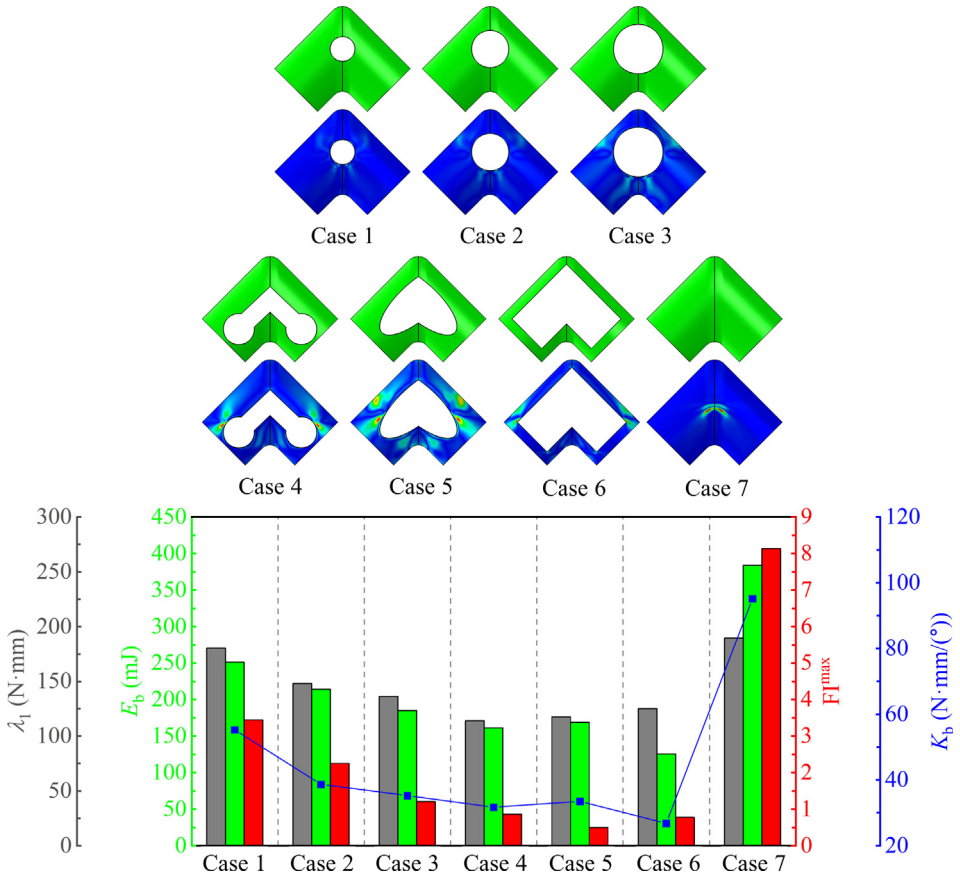

Fig. 4 Effects of cutout size and shape on $\lambda_1, E_b, \mathrm{FI}^{max}$, and K_b of RA-WCTH.

'opt' represents the optimal result in the single-objective optimization, and the superscript 'int' represents the result of the initial structure.$\boldsymbol{X}$ is the element density vector;x_e is the relative density of the e-th element, with candidate values of 1 (existing) or 0 (non-existent, i.e., cutout); N is the total number of elements;$\boldsymbol{F}$ is the global mechanical load vector;$\boldsymbol{K}$ and $\boldsymbol{K}_\sigma$ are the global stiffness matrix and stress stiffness matrix;$\boldsymbol{U}$ and $\boldsymbol{U}_1$ are, respectively, the global displacement vector obtained by solving the static finite element equilibrium equations and the global displacement vector obtained by solving the linear buckling finite element equilibrium equations (first-order buckling mode).

3.2. Sensitivity analysis model

BESO, as a gradient-based optimization model, achieves the addition or removal of elements based on the element sensitivity α_e derived from the differentiated objective function $T(\boldsymbol{X})$:

$$\alpha_e = \frac{\partial T(\boldsymbol{X})}{\partial x_e} \tag{7}$$

In this study, compliance $C(\boldsymbol{X})$ (which is equal to the sum of the elastic strain energy of all elements in the structure, denoted as the strain energy $E_b(\boldsymbol{X})$ stored after deformation) is equivalently used to represent the first optimization objective, the bending stiffness $K_b(\boldsymbol{X})$. It is specifically clarified that using this concept to equivalently represent the overall stiffness of a macrostructure has been reported in numerous topology optimization studies.[19,51] Similarly, for the RA-WCTH with different cutout designs, $K_b(\boldsymbol{X})$ has a clear linear relationship with $C(\boldsymbol{X})$, as detailed in Fig. 4. The sensitivity $\alpha_e^{C(X)}$ of $C(\boldsymbol{X})$ is expressed as follows:

$$\alpha_e^{C(X)} = \frac{\partial C(\boldsymbol{X})}{\partial x_e} = p x_e^{p-1} \boldsymbol{u}_e^{\mathrm{T}} \boldsymbol{k}_e^0 \boldsymbol{u}_e = p \frac{E_e}{x_e} \tag{8}$$

where p is the penalty exponent, typically set to 3. $\boldsymbol{u}_e$ is the nodal displacement vector of the e-th element, and $\boldsymbol{k}_e^0$ is the stiffness matrix of the solid element (i.e., $x_e = 1$), obtained by processing the ABD matrix through shape functions and the assembly matrix. The processed sensitivity includes a term, $x_e^p \boldsymbol{u}_e^{\mathrm{T}} \boldsymbol{k}_e^0 \boldsymbol{u}_e$, whose magnitude is equal to the strain energy E_e of the element.[43]

The critical buckling load $\lambda_1(\boldsymbol{X})$ is the second optimization objective. Extract the finite element equilibrium equations for linear buckling analysis from Eq. (6):

$$(\boldsymbol{K} + \lambda_1 \boldsymbol{K}_\sigma) \boldsymbol{U}_\mathrm{m} = 0 \tag{9}$$

Convert it into a function of λ_1 and x_e:

$$f(\lambda_1, x_e) = \sum_e^n \boldsymbol{u}_{e,1}^{\mathrm{T}} \boldsymbol{k}_e \boldsymbol{u}_{e,1} + \lambda_1 \sum_e^n \boldsymbol{u}_{e,1}^{\mathrm{T}} \boldsymbol{k}_{e,\sigma} \boldsymbol{u}_{e,1} \tag{10}$$

During the iterative process of buckling topology optimization, regions composed of low-density elements are prone to pseudo-buckling mode phenomena, resulting in final optimization outcomes that deviate from reality. Neves et al. discovered that this phenomenon is caused by the stress stiffness matrix $\boldsymbol{k}_{e,\sigma}$ of low-density elements being significantly larger than their stiffness matrix $\boldsymbol{k}_e$.[38] In finite element analysis and sensitivity calculations, $\boldsymbol{k}_{e,\sigma}$ is artificially neglected. This direct approach stabilizes the optimization process but induces numerical oscillations. Consequently, Bendsøe and Sigmund developed smooth interpolation functions for both $\boldsymbol{k}_{e,\sigma}$ and $\boldsymbol{k}_e$ to compensate for the numerical discrepancies between these two stiffness matrices of low-density elements during the evolutionary process.[19] The specific forms are as follows:

$$\begin{cases} E_{\boldsymbol{k}_e} = \left(x_{\min} + (1 - x_{\min})x_e^p\right)E^0 \\ E_{\boldsymbol{k}_{e,\sigma}} = x_e^p E^0 \end{cases} \tag{11}$$

Here, $E_{\boldsymbol{k}_e}$ and $E_{\boldsymbol{k}_{e,\sigma}}$ are the Young's moduli corresponding to $\boldsymbol{k}_e$ and $\boldsymbol{k}_{e,\sigma}$, respectively. E_e^0 is the Young's modulus of a solid element. The differential expressions for $\boldsymbol{k}_e$ and $\boldsymbol{k}_{e,\sigma}$ are as follows:

$$\begin{cases} \frac{\partial \boldsymbol{k}_e}{\partial x_e} = (1 - x_{\min})px_e^{p-1}\boldsymbol{k}_e^0 \\ \frac{\partial \boldsymbol{k}_{e,\sigma}}{\partial x_e} = px_e^{p-1}\boldsymbol{k}_e^0 \end{cases} \tag{12}$$

By taking the partial derivative of Eq. (10) with respect to x_e based on the chain rule and substituting Eq. (12) into it, the sensitivity expression of $\lambda_1(\boldsymbol{X})$ is obtained:

$$\frac{\partial \lambda_1(\boldsymbol{X})}{\partial x_e} = \frac{\partial f}{\partial x_e} \Big/ \frac{\partial f}{\partial \lambda_1} = \frac{(1 - x_{\min} + \lambda_1)px_e^{p-1}\boldsymbol{u}_{e,1}^{\mathrm{T}}\boldsymbol{k}_e^0\boldsymbol{u}_{e,1}}{\boldsymbol{U}_1^{\mathrm{T}}\boldsymbol{K}_\sigma\boldsymbol{U}_1} \tag{13}$$

where the buckling mode, $\boldsymbol{U}_1$, is normalized by $\boldsymbol{k}_\sigma$, therefore:

$$\boldsymbol{U}_1^{\mathrm{T}}\boldsymbol{K}_\sigma\boldsymbol{U}_1 = 1 \tag{14}$$

Similar to what is shown in Eq. (8), the strain energy of the e-th element in the critical buckling mode can be defined as

$$E_{e,1} = x_e^p\boldsymbol{u}_{e,1}^{\mathrm{T}}\boldsymbol{k}_e^0\boldsymbol{u}_{e,1} \tag{15}$$

By substituting Eq. (14) and Eq. (15) into Eq. (13), the final expression for the sensitivity of $\lambda_1(\boldsymbol{X})$ is obtained:

$$\alpha_e^{\lambda_1(\boldsymbol{X})} = (1 - x_{\min} + \lambda_1)p\frac{E_{e,1}}{x_e} \tag{16}$$

where $x_{\min}$ is set to 0.

Aggregating discrete element variables into a single continuous function using the P-norm is a primary method for deriving the sensitivity of global stress levels with respect to element density. This approach is applicable to frameworks such as SIMP, BESO, and Level-Set.[52–55] Recently, it was found that this method is also suitable for deriving the sensitivity of the failure index in woven composites,[35] as shown below:

$$\mathrm{FI}^{\mathrm{PN}}(\boldsymbol{X}) = \left(\sum_{e=1}^{N}\mathrm{FI}_e^p(\boldsymbol{X})\right)^{1/p} \tag{17}$$

where $\mathrm{FI}_e^p(\boldsymbol{X})$ is the failure index at the centroid of the e-th element, and p is the exponent of the failure index norm. When $p = 1$, the P-norm gives the average failure index, and as $p \to \infty$, the P-norm approaches the maximum failure index $\mathrm{FI}^{\max}(\boldsymbol{X})$. Excessively large p values can cause numerical oscillations. Therefore, the selection of p should be cautious to avoid deteriorating the smoothness of the problem while sufficiently approximating the maximum failure index. Based on experience in topology optimization with stress constraints,[53] the p value is generally recommended to be between 3 and 6.

Using the chain rule, the derivative of $\mathrm{FI}^{\mathrm{PN}}(\boldsymbol{X})$ with respect to the e-th design variable x_e equals the element sensitivity of the failure index:

$$\alpha_e^{\mathrm{FI}(\boldsymbol{X})} = \frac{\partial \mathrm{FI}^{\mathrm{PN}}(\boldsymbol{X})}{\partial \mathrm{FI}_e(x_e)}\left(\frac{\partial \mathrm{FI}_e(x_e)}{\partial \boldsymbol{N}_e(x_e)}\right)^{\mathrm{T}}\frac{\partial \boldsymbol{N}_e(x_e)}{\partial x_e} \tag{18}$$

where $\mathrm{FI}_e(x_e)$ is equal to the first equation in Eq. (2), and $\boldsymbol{N}_e(x_e) = \left[N_x, N_y, N_{xy}\right]^{\mathrm{T}}$.

According to the definition in Eq. (17), $\partial \mathrm{FI}^{\mathrm{PN}}(\boldsymbol{X})/\partial \mathrm{FI}_e(x_e)$ can be calculated as:

$$\frac{\partial \mathrm{FI}^{\mathrm{PN}}(\boldsymbol{X})}{\partial \mathrm{FI}_e(x_e)} = \left(\sum_{i=1}^{N}\left(\mathrm{FI}_e(x_e)\right)^P\right)^{\left(\frac{1-P}{P}\right)}\left(\mathrm{FI}_e(x_e)\right)^{P-1} \tag{19}$$

The derivatives of $\mathrm{FI}_e(x_e)$ with respect to the stress components, $\left(\partial \mathrm{FI}_e(x_e)/\partial \boldsymbol{N}_e(x_e)\right)^{\mathrm{T}}$, are

$$\begin{cases} \frac{\partial \mathrm{FI}_e(x_e)}{\partial N_x(x_e)} = f_1 + 2f_{11}N_x(x_e) + f_{12}N_y(x_e) \\ \frac{\partial \mathrm{FI}_e(x_e)}{\partial N_y(x_e)} = f_1 + 2f_{11}N_y(x_e) + f_{12}N_x(x_e) \\ \frac{\partial \mathrm{FI}_e(x_e)}{\partial N_{xy}(x_e)} = 2f_{33}N_{xy}(x_e) \end{cases} \tag{20}$$

Based on the above analysis of the failure mechanism of RA-WCTH, it was deter-mined that failure occurs only at the central position of the structure. Here, a double-layer plain-woven composite material with symmetric layup is used, where the submatrix $\boldsymbol{B}$ in the ABD matrix is equal to zero, which implies that Eq. (1) can be reduced to

$$\boldsymbol{N}_e(x_e) = \boldsymbol{A}_e(x_e)\boldsymbol{\varepsilon}_e(x_e) \tag{21}$$

where $\boldsymbol{A}_e(x_e)$ is a submatrix of the ABD matrix and $\boldsymbol{N}_e(x_e) = [N_x(x_e), N_y(x_e), N_{xy}(x_e)]^{\mathrm{T}}$ is the section stress of element. Middle plane strain of element ($\boldsymbol{\varepsilon}_e(x_e) = [\varepsilon_x(x_e), \varepsilon_y(x_e), \gamma_{xy}(x_e)]^{\mathrm{T}}$) can be obtained by the dot product of the in-plane strain–displacement matrix $\boldsymbol{M}$ and the nodal displacement vector $\boldsymbol{u}_e(x_e) = [u_x(x_e), u_y(x_e), u_z(x_e)]^{\mathrm{T}}$:

$$\boldsymbol{\varepsilon}_e(x_e) = \boldsymbol{M}\boldsymbol{u}_e(x_e) \tag{22}$$

By combining $\boldsymbol{K}\boldsymbol{U} = \boldsymbol{F}$ from Eq. (6), along with Eq. (21) and Eq. (22), $\boldsymbol{N}_e(x_e)$ is derived as follows:

$$\frac{\partial \boldsymbol{N}_e(x_e)}{\partial x_e} = px_e^{p-1}\boldsymbol{A}_e\boldsymbol{\varepsilon}_e - \boldsymbol{A}_e\boldsymbol{M}\boldsymbol{L}_e\boldsymbol{K}^{-1}\frac{\partial \boldsymbol{K}}{\partial x_e}\boldsymbol{U} \tag{23}$$

Substituting Eq. (23) into Eq. (18), the sensitivity expression of $\mathrm{FI}^{\mathrm{PN}}(\boldsymbol{X})$ with respect to x_e is finally obtained as follows:

$$\alpha_e^{\mathrm{FI}(\boldsymbol{X})} = px_e^{p-1}\boldsymbol{A}_e\boldsymbol{\varepsilon}_e\frac{\partial \mathrm{FI}^{\mathrm{PN}}(\boldsymbol{X})}{\partial \mathrm{FI}_e}\left(\frac{\partial \mathrm{FI}_e}{\partial \boldsymbol{N}_e}\right)^{\mathrm{T}} - \boldsymbol{\xi}^{\mathrm{T}}\frac{\partial \boldsymbol{K}}{\partial x_i}\boldsymbol{U} \tag{24}$$

where ξ is obtained by solving the adjoint equation as shown in Eq. (25).

$$\boldsymbol{K}\boldsymbol{\xi} = \sum_{e=1}^{n}\frac{\partial \mathrm{FI}^{\mathrm{PN}}(x_e)}{\partial \mathrm{FI}(x_e)}\boldsymbol{L}_e^{\mathrm{T}}\boldsymbol{M}^{\mathrm{T}}\boldsymbol{A}_e^{\mathrm{T}}(x_e)\frac{\partial \mathrm{FI}_e(x_e)}{\partial \boldsymbol{N}_e(x_e)} \tag{25}$$

The adjoint vector $\boldsymbol{\xi}$ plays a crucial role in optimizing stress-constrained topology optimization models.[53] However, solving for $\boldsymbol{\xi}$ requires the establishment of an additional finite element model, along with redefined boundary conditions based on Eq. (25), followed by further computation. This process, which must be repeated in every iteration of the topology optimization, significantly increases computational costs-especially for complex structures with large mesh counts. To address this challenge, Some studies have attempted to neglect the adjoint term $\boldsymbol{\xi}$ in stress topology optimization of deployable shell structures, achieving significant results.[46] Given the large number of elements of the RA-WCTH macro model, this method is also adopted in the present study. Ignoring the adjoint terms($\boldsymbol{\xi} = \mathbf{0}$) can improve computational efficiency, but its impact varies significantly across different optimization problems. In two-dimensional planar problems, this approach leads to an average error of more than 50%.[56] However, in the stress topology optimization problem of 3D shell elements, this method demonstrates high optimization accuracy. S. Ferraro first proved that, in the stress topology optimization of 3D plates, the impact of ignoring the adjoint vector on the final structural configuration is minimal, with the maximum Von Mises stress error around 7%.[46] This method also exhibits good convergence and significant stress level reduction when applied to the classical deployable structure, Tape-spring (with complex geometric deformations). In summary, whether ignoring the adjoint vector in stress topology optimization models is applicable to more types of structures still lacks sufficient research and verification. Therefore, the limitations of the method presented in this paper need to be stated, and future research should focus on the topology optimization of 3D shell element stress (failure index) with consideration of the adjoint vector.

3.3. Multi-objective topology optimization framework and implementation

Fig. 5 illustrates the implementation method of multi-objective topology optimization. The execution process is achieved by integrating the ABAQUS 2023 with Python code. First, two finite element models of the RA-WCTH were established in the ABAQUS/CAE environment for nonlinear folding analysis and linear buckling analysis, respectively. The specific parameters of the models are detailed in Sec. 2. The objective function values $C(\boldsymbol{X})$ and $\lambda_1(\boldsymbol{X})$, as well as the constraint function value $\mathrm{FI}(\boldsymbol{X})$ and information at the centroid of each element, were extracted from the two independent result files (.odb). This includes the failure index, strain energy, and sectional stress of each element when the RA-WCTH is folded to 45°; and the strain energy of each element in the first buckling mode of the RA-WCTH. These values are substituted into Eqs. (8), (16), (18), (19) and (20) to calculate the sensitivities of each objective and constraint function relative to the design variables, $\alpha_e^{C(\boldsymbol{X})}$, $\alpha_e^{E_b(\boldsymbol{X})}$, and $\alpha_e^{\mathrm{FI}(\boldsymbol{X})}$. To balance the two optimization objectives and the constraint during the optimization process, this study uses a linear weighted sum method to aggregate the three independent sensitivities. Before aggregation, they were normalized to a range of 0–1:

$$\begin{cases} \bar{\alpha}_e^{C(\boldsymbol{X})} = \dfrac{\alpha_e^{C(\boldsymbol{X})} - \alpha_{e,\min}^{C(\boldsymbol{X})}}{\alpha_{e,\max}^{C(\boldsymbol{X})} - \alpha_{e,\min}^{C(\boldsymbol{X})}} \\ \bar{\alpha}_e^{\lambda_1(\boldsymbol{X})} = \dfrac{\alpha_e^{\lambda_1(\boldsymbol{X})} - \alpha_{e,\min}^{\lambda_1(\boldsymbol{X})}}{\alpha_{e,\max}^{\lambda_1(\boldsymbol{X})} - \alpha_{e,\min}^{\lambda_1(\boldsymbol{X})}} \\ \bar{\alpha}_e^{\mathrm{FI}(\boldsymbol{X})} = \dfrac{\alpha_e^{\mathrm{FI}(\boldsymbol{X})} - \alpha_{e,\min}^{\mathrm{FI}(\boldsymbol{X})}}{\alpha_{e,\max}^{\mathrm{FI}(\boldsymbol{X})} - \alpha_{e,\min}^{\mathrm{FI}(\boldsymbol{X})}} \end{cases} \tag{26}$$

where the subscripts 'max' and 'min' represent the maximum and minimum values of the sensitivities among all elements, respectively.

The aggregated sensitivity expression is as follows:

$$\alpha_e = w_1 \cdot \bar{\alpha}_e^{C(\boldsymbol{X})} + w_2 \cdot \bar{\alpha}_e^{\lambda_1(\boldsymbol{X})} - w_3 \cdot \bar{\alpha}_e^{\mathrm{FI}(\boldsymbol{X})} \tag{27}$$

where the values and meanings of the weighting factors are consistent with those in Eq. (6).

Observing the sensitivity distribution contour plots in Fig. 5, it is evident that the peak values of the three sensitivities overlap significantly but carry different meanings. The first two imply that to achieve higher stiffness and critical buckling load for the RA-WCTH, the highlighted region's elements need to be retained. The element evolution strategy regarding the failure index is the opposite. The magnitude of the weighting factors in Eq. (27) determines the emphasis on individual optimization objectives, while the sign determines the evolution direction dominated by either retaining or removing elements.

To ensure mesh independence and avoid the appearance of checkerboard patterns, the following sensitivity filtering method was employed in this study:

$$\hat{\alpha}_e = \frac{\sum_{j=1}^{N} w(r_{ej})\alpha_j}{\sum_{j=1}^{N} w(r_{ej})} = \sum_{j=1}^{N} \eta_j \alpha_j \tag{28}$$

$$w(r_{ej}) = \max(0, r_{\min} - r_{ej}) \tag{29}$$

where r_{ej} is the distance between the e-th element and j-th element; α_j is the aggregated sensitivity of the element calculated from Eq. (27); $w(r_{ej})$ is the weighting function used to average the original sensitivities; $r_{\min}$ is the filter radius; the weighting factor η_j is independent of the sensitivities and is precomputed before the optimization iterations; this filter is applied once in each iteration.

To improve the convergence of the optimization process, the current sensitivity is averaged with its historical information:

$$\alpha_e = \frac{\hat{\alpha}_e^{\mathrm{iter}} + \hat{\alpha}_e^{\mathrm{iter}-1}}{2} \tag{30}$$

where iter is the current iteration number.

BESO typically starts with a fully structured design and gradually reduces the structure's volume by updating the element states. During the iterations, the target volume for the next iteration $V^{\mathrm{iter}+1}(\boldsymbol{X})$ is determined based on the current volume $V^{\mathrm{iter}}(\boldsymbol{X})$ and the evolution rate ert.

$$V^{\mathrm{iter}+1}(\boldsymbol{X}) = (1 - \mathrm{ert})V^{\mathrm{iter}}(\boldsymbol{X}) \tag{31}$$

All element information (element sequence number and corresponding sensitivities α_e) is transferred to the BESO optimizer. Fig. 5 shows the pseudocode for the BESO optimizer using the bisection method to update the design variables. In the iter-th iteration, the intermediate threshold $\alpha_{\mathrm{th}}^{\mathrm{iter}}$ between

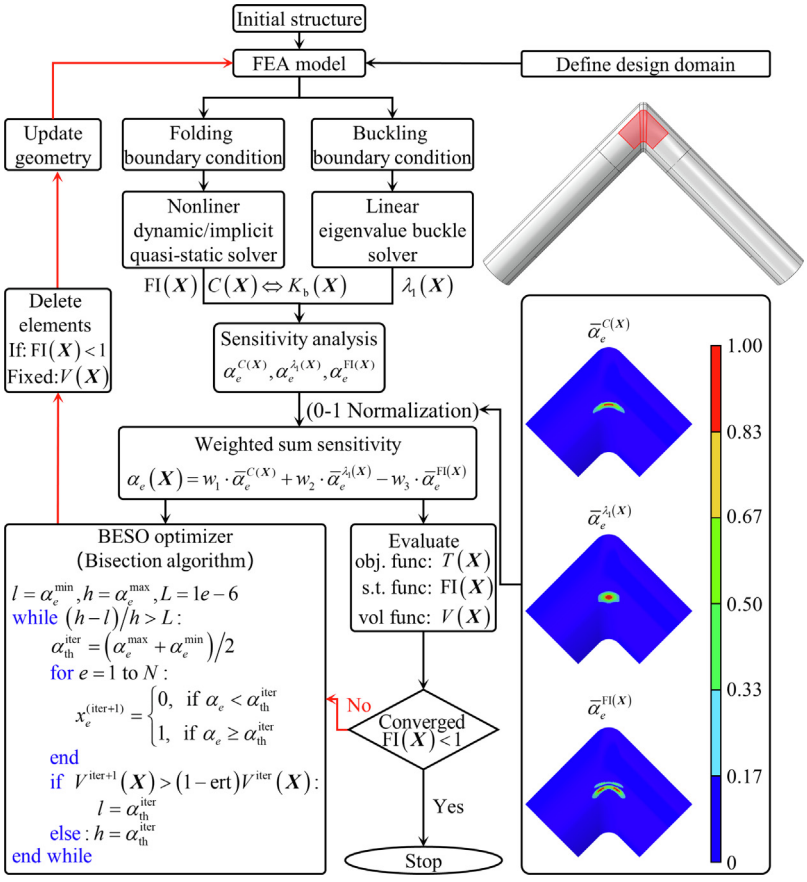

Fig. 5 Multi-objective BESO implementation framework.

the maximum element sensitivity $\alpha_e^{\max}$ and the minimum element sensitivity $\alpha_e^{\min}$ is first determined. All elements are then traversed, and the design variables $x_e^{\text{iter}+1}$ of elements with sensitivity values less than $\alpha_{\text{th}}^{\text{iter}}$ are updated to 0, while the design variables of the remaining elements are updated to 1. This process continues until the current target volume $(1-\text{ert})V^{\text{iter}}(\boldsymbol{X})$ is met. Based on the current distribution of design variables, elements of the RA-WCTH are removed to update the geometric model. Before the multi-objective optimization begins in this study, a very small target volume and evolution rate (ert) are set to allow BESO to slowly remove elements from the RA-WCTH. When the structure meets the constraint condition $\text{FI}(\boldsymbol{X}) < 1$, the target volume is reset to the current volume of the structure. This approach halts further element reduction in the RA-WCTH by BESO, thus maximizing the preservation of stiffness and critical buckling load.

The automatic execution and iterative cycling of a series of modules, including finite element model calculations, post-processing of computational results, data transfer, BESO optimizer determination of optimal material distribution, and geometric model updates, are implemented by Python code. The optimization terminates when the failure index of the RA-WCTH satisfies the constraint conditions and the optimization objectives meet the convergence criteria, as given by Eq. (32). In this study, the value of M is set to 5.

$$\epsilon = \frac{\left|\sum_{i=1}^{M}\left(T_{\text{iter}-i+1}(\boldsymbol{X}) - T_{\text{iter}-i+1-M}(\boldsymbol{X})\right)\right|}{\sum_{i=1}^{M} T_{\text{iter}-i+1}(\boldsymbol{X})} \leqslant 0.01 \tag{32}$$

4. Optimization results

4.1. Single-objective optimization results

The switch between multi-objective and single-objective algorithms can be achieved by simply modifying the sensitivity weighting factors (w_1, w_2, w_3). Before initiating the multi-objective optimization, Fig. 6 demonstrates the RA-WCTH cutout's evolution under the influence of a single sensitivity. Fig. 6(a) to (c) respectively illustrate the topology optimization results of RA-WCTH under the exclusive action of the failure index sensitivity $\bar{\alpha}_e^{\text{FI}(\boldsymbol{X})}(0,0,1)$, the bending stiffness sensitivity $\bar{\alpha}_e^{C(\boldsymbol{X})}(1,0,0)$, and the critical buckling load sensitivity $\bar{\alpha}_e^{\lambda_1(\boldsymbol{X})}(0,1,0)$.

As shown in Fig. 6(a), the element removal in RA-WCTH begins at the concentration area of $\text{FI}(\boldsymbol{X})$, and the cutout formation spreads outward from this center. Once the constraint $\text{FI}^{\max}(\boldsymbol{X}) < 1$ is satisfied, the volume of the RA-WCTH no longer decreases, and the cutout shape becomes stable. After minor shape adjustments, the final cutout takes an approximately elliptical form. In Fig. 6(b), the element removal starts with the elements contributing the least to the bending stiffness $K_{\text{b}}(\boldsymbol{X})$. Due to the absence of failure index sensitivity considerations, the failure index of RA-WCTH remains high throughout the iterations compared to Fig. 6(a). In this scenario, a substan-

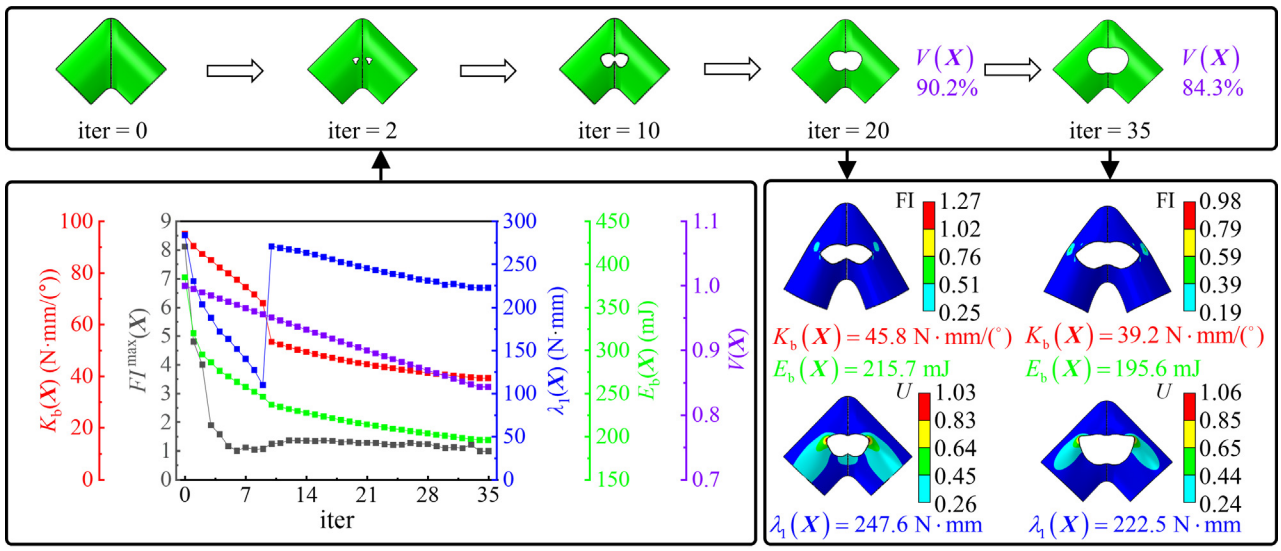

(a) Optimization results with sensitivity analysis on FI^{max}

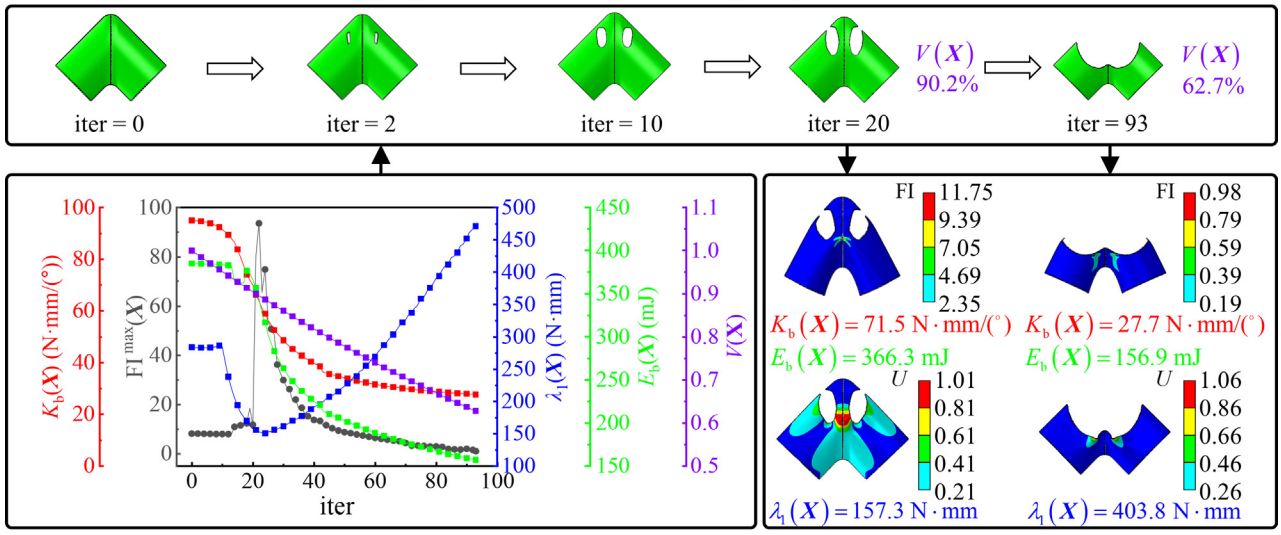

(b) Optimization results with sensitivity analysis on K_b

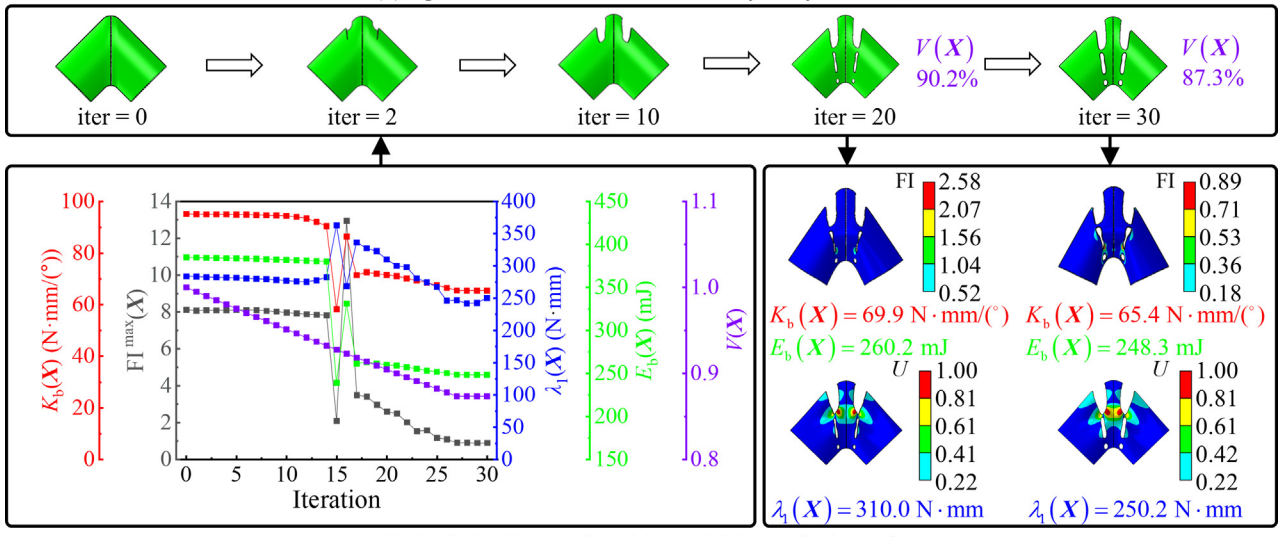

(c) Optimization results with sensitivity analysis on λ_1

Fig. 6 Optimization results of RA-WCTH where only a single sensitivity analysis (FI^{max}, $K_b$or λ_1).

tial number of elements must be removed to extend the cutout from top to bottom, thereby entirely eliminating the region with a high failure index—an area that also contributes the most to overall stiffness and strain energy (see Fig. 5). As a result, the RA-WCTH meets the constraint conditions but ends up with the lowest volume fraction (62.7%) and the poorest bending stiffness. Interestingly, this extensive cutout triggers a major shift in the RA-WCTH's buckling mode, leading to a critical buckling load far exceeding those shown in Fig. 6(a) and Fig. 6(c). In Fig. 6(c), the element removal also starts with the elements that contribute the least to the critical buckling load $\lambda_1(\boldsymbol{X})$. Ultimately, RA-WCTH achieves a series of discontinuous elongated cutouts while satisfying the failure constraints. This optimization result preserves the central region that contributes the most to $\lambda_1(\boldsymbol{X})$, thereby exhibiting superior critical buckling load, bending stiffness, and elastic strain energy compared to Fig. 6(a).

In order to further validate the accuracy of the single-objective topology optimization model, a comparison was made among the three optimization outcomes at the 20th iteration, where the volume fraction remained identical. Each single-objective model exhibited a markedly stronger performance in its respective optimization objective relative to the other two models, underscoring the efficiency of the BESO optimization code and the reliability of the sensitivity model. Several preliminary conclusions emerge from these observations: preserving the central region furnishes RA-WCTH with higher bending stiffness and elastic strain energy, whereas a larger cutout may trigger abrupt shifts in local buckling modes that result in unpredictable variations in the critical buckling load. Consequently, relying solely on single-objective topology optimization impedes the attainment of an optimal RA-WCTH cutout, thus highlighting the need for guidance from all three sensitivities and careful consideration of weighting ratios to achieve a fully optimized outcome.

4.2. Multi-objective optimization results

Subsequently, two types of bi-objective topology optimization studies were conducted on RA-WCTH: maximizing bending stiffness and minimizing the failure index until the maximum failure index across all elements was less than 1, corresponding to the weight coefficients (w_1, 0, w_3) in Eq. (6); and maximizing the critical buckling load and minimizing the failure index until the maximum value across all elements was less than 1, corresponding to the weight coefficients (0, w_2, w_3) in Eq. (6).

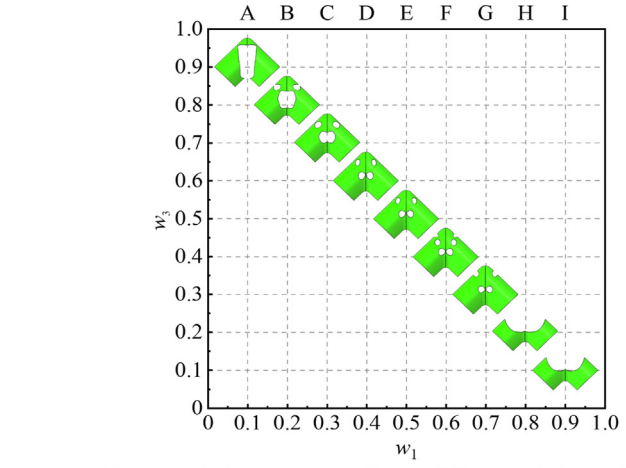

(a) Cutout designs corresponding to different weight combinations

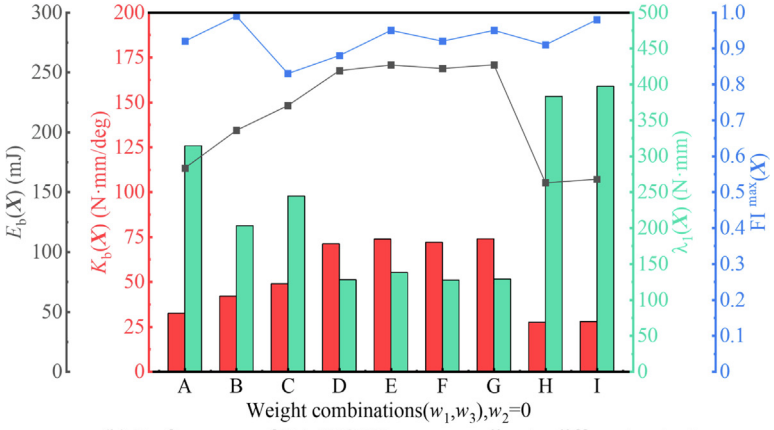

(b) Performance of RA-WCTH corresponding to different cutouts

Fig. 7 Effect of weighting factors on optimization results (bi-objective: minimum FI^{max} and maximum K_b).

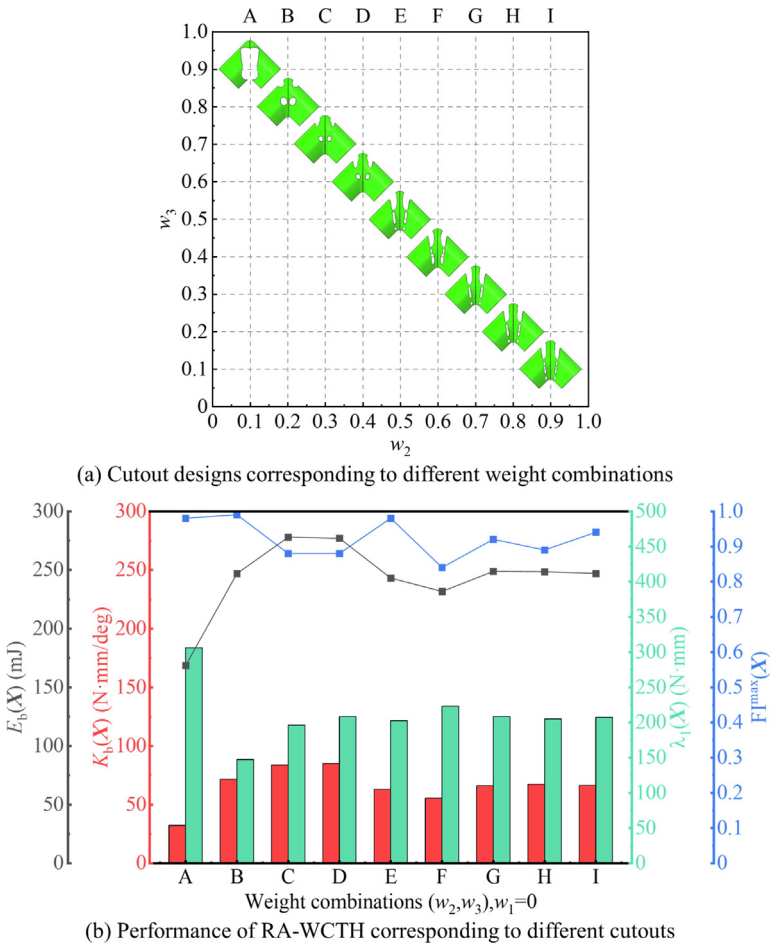

Fig. 8 Effect of weighting factors on optimization results (bi-objective: minimum FI^{max} and maximum λ_1).

Fig. 7(a) shows the optimized cutout designs of RA-WCTH for nine different weight coefficient ratios for the first single-objective optimization problem, and Fig. 7(b) presents the corresponding performance for each optimized design. The results indicate that as the bending stiffness weight factor increases and the failure index weight factor decreases, the cutout edges exhibit a trend of initially contracting towards the center and then expanding upwards. Along with this trend, the optimized bending stiffness shows a pattern of initially increasing and then decreasing. Fig. 8(a) and (b) show the nine optimized designs and corresponding performance for the second single-objective optimization problem. As the buckling load weight factor increases and the failure index weight factor decreases, the cutout edges first contract towards the center and then begin to expand longitudinally on both sides of the midpoint, eventually stabilizing in a discontinuous strip-like form.

It is evident that both Fig. 7 and Fig. 8 show a relatively stable interval. Within this interval, the cutout designs and objective function values are very close, specifically (0.4, 0.0, 0.6) – (0.7, 0.0, 0.3) and (0.0, 0.5, 0.5) – (0.0, 0.9, 0.1), respectively. The first interval exhibited the best bending stiffness performance and the worst critical buckling load, while the second interval showed the opposite. This demonstrates the effectiveness of the topology optimization model presented in this paper for single-objective optimization problems.

Finally, the multi-objective optimization problem represented by Eq. (6) is formally solved, and the influence of the synergistic effect of the three weighting factors (w_1, w_2, w_3) on the topology optimization results is analyzed. Fig. 9(b) presents the response values of the optimization objectives and constraint functions for the 45 optimized designs. Notably, the maximum failure index for all designs is below 1, and a clear Pareto front is projected onto the horizontal plane $K_b(\boldsymbol{X}) - \lambda_1(\boldsymbol{X})$. Fig. 9(c) provides an enlarged view of this Pareto front, highlighted with gray curves. Based on the similarities in the location, quantity and shape of the cutouts, the 45 optimized designs are categorized into seven clusters, each distinguished by a different color. Clusters 1, 2, 5, 6, and 7 contribute to the construction of the Pareto front, while Clusters 3 and 4 reside within the envelope region. A total of eleven representative designs (A–K) are selected to illustrate the general patterns of notch variations. Along the Pareto front, it is observed that improving one objective necessitates compromising another. Specifically, Cluster 1 is closest to the upper limit of $\lambda_1(\boldsymbol{X})$, Cluster 6 is nearest to the upper limit of $K_b(\boldsymbol{X})$, and Clusters 5 and 7 lie between these two extremes, reflecting a trade-off between the two optimization objectives. Taking Design E from Cluster 7 as the central point of the Pareto front, the designs distributed to the left tend to remove material from the RA-WCTH's strain concentration regions and their surroundings, resulting in cutouts with larger surface

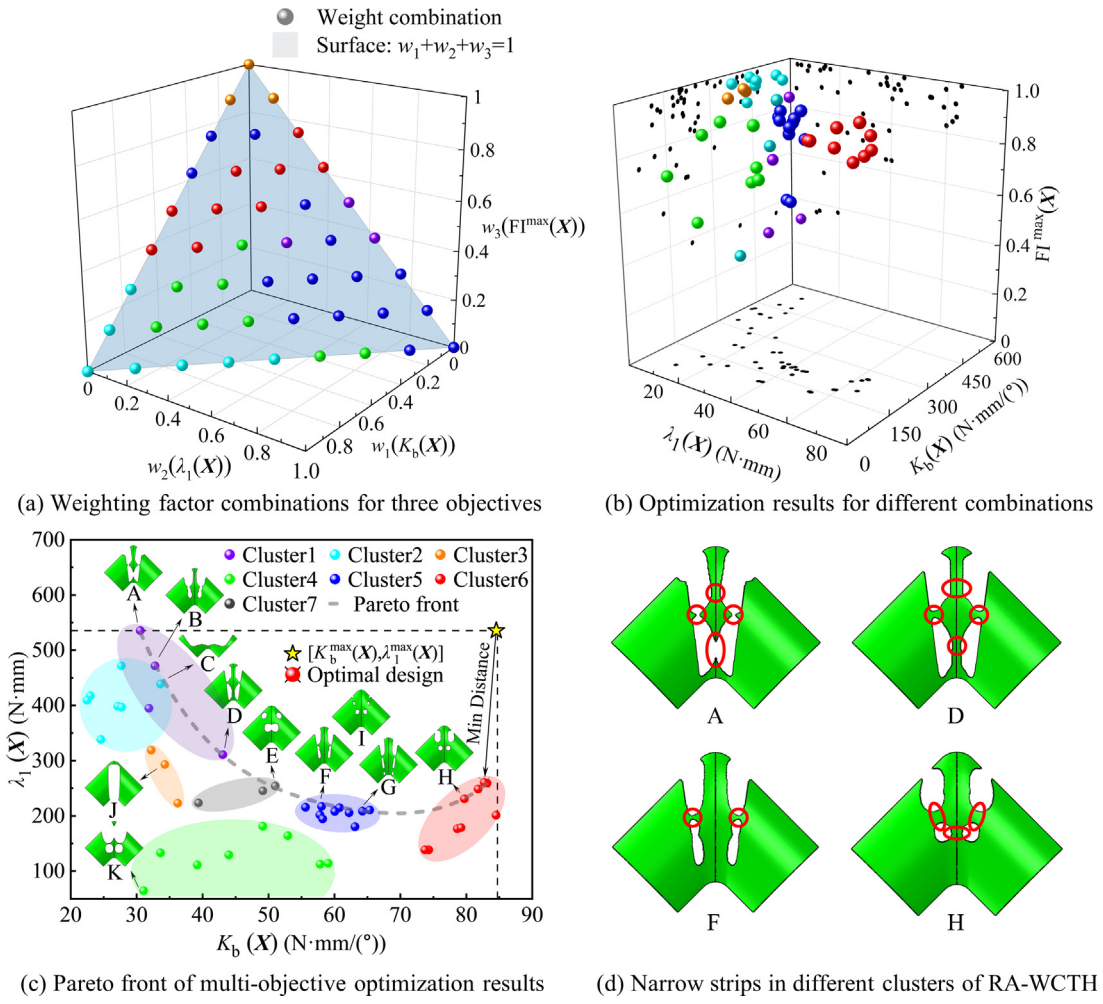

(a) Weighting factor combinations for three objectives

(b) Optimization results for different combinations

(c) Pareto front of multi-objective optimization results

(d) Narrow strips in different clusters of RA-WCTH

Fig. 9 Multi-objective topology optimization results.

areas. This configuration induces a transition in the RA-WCTH's original buckling mode, leading to an optimized outcome with high critical buckling load but low bending stiffness.

Conversely, designs distributed to the right of Design E favor retaining a larger area of material at the RA-WCTH center and symmetrically arranging discontinuous cutouts from top to bottom on both sides. This results in an optimized configuration with low critical buckling load but high bending stiffness. These observations are consistent with the patterns demonstrated in the earlier single-objective and dual-objective optimization results. Although the current Pareto front's continuity is not perfect, it is believed that further reducing the sampling interval of the weight factors will enrich and clarify the Pareto front, which will be addressed in future research. Nevertheless, the elucidated patterns already provide sufficient theoretical foundations for engineering design. Utilizing the ideal point method,[57] an imaginary utopian point is constructed in Fig. 9(b) based on $K_b^{\max}(\boldsymbol{X})$ and $\lambda_1^{\max}(\boldsymbol{X})$. The optimized design with the shortest Euclidean distance to this utopian point on the Pareto front is considered the optimal design for RA-WCTH multi-objective topology optimization, as illustrated by Design I in Fig. 9(a).

Scale effects are critical considerations in the fabrication of thin-walled structures using composite laminated plates. Different types and size ranges of laminated plates may exhibit varying scale effects. For example, unidirectional composites with sizes ranging from 50.8 mm to 12.7 mm demonstrate increased stiffness and strength as size decreases. In contrast, the $[45]_2$ Astroquartz® laminates used in this study exhibit the opposite trend within the range of 1 to 15 wavelengths

Table 5 Width range of narrow strip on RA-WCTH.

Cluster	1	2	3	4	5	6	7
Max width (mm)	2.16	0	0	2.98	1.29	3.32	3.91
Min width (mm)	1.13	0	0	0.13	0.48	1.03	0.17
Average width (mm)	1.74	0	0	1.19	0.86	2.19	2.46

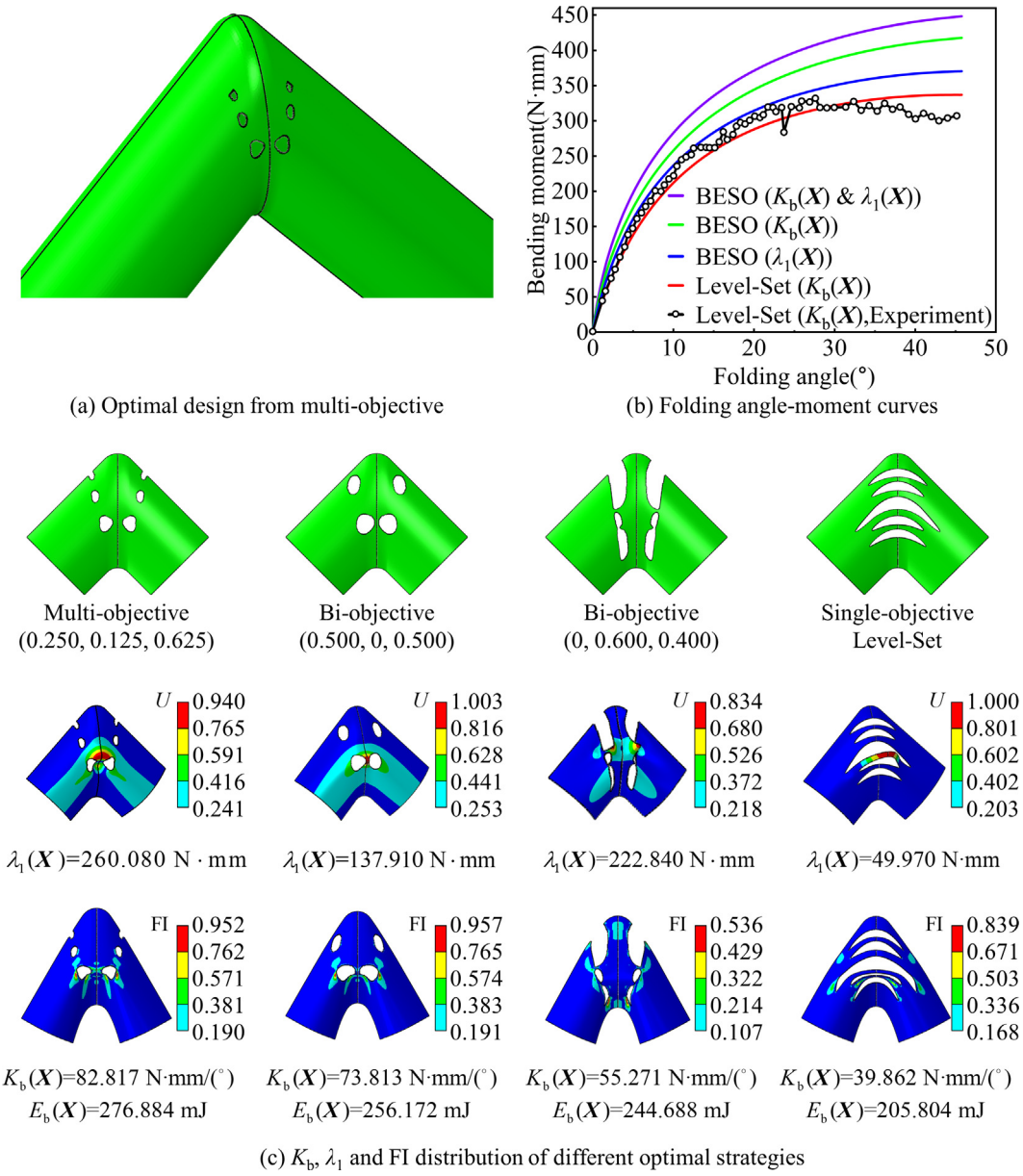

(a) Optimal design from multi-objective

(b) Folding angle-moment curves

(c) K_b, λ_1 and FI distribution of different optimal strategies

Fig. 10 Comparison of optimization results among multi-objective BESO, bi-objective BESO and Level-Set.[40]

(unit wavelength: 1 mm).[47] This discrepancy is attributed to defects such as the heat-affected zone, fiber pull-out, delamination, and dry spots generated during the laser cutting process. Therefore, it is essential to evaluate the dimensions of the narrow strips in all optimized designs, as shown in Fig. 9(d), to prevent performance degradation in practical engineering applications due to scale effects. Table 5 summarizes the maximum, minimum, and average widths of the strips for all designs within the seven clusters. In Clusters 2 and 3, which consist of designs similar to Design J and Design C in Fig. 9 (c), no narrow strips were observed.

In Clusters 4, 5 and 7 designs exhibited strips with widths smaller than one wavelength. Considering the average machining precision of the laser cutter, such designs will be excluded. The optimal design I has a minimum strip width of 2.34 mm, which is within the machining precision range.

Table 6 Size-scaling parameters of $[45]_2$ laminates.[47]

Strip width (mm)	F_3 (N/mm)	F_{1c} (N/mm)	β
15.00	14.55	34.50	1.00
3.00	10.34	29.07	0.90
2.00	6.91	25.94	0.74
1.50	6.76	25.70	0.72
1.00	4.27	19.37	0.52

Note: Wavelength of $[45]_2$ Astroquartz® laminate: 1 mm.

Next, this multi-objective optimization result is compared with the two bi-objective BESO topology optimization results. The results are exciting. Fig. 10(b) shows the bending moment evolution curves of RA-WCTH under three different optimization schemes as the folding angle increases.

The RA-WCTH optimized by multi-objective BESO exhibits the highest bending stiffness, with its corresponding purple curve having the largest enclosed area, indicating that when folded to 45°, the RA-WCTH stores the most elastic strain energy and thus possesses the strongest self-deployment capability. Fig. 10 (c) presents the failure index distribution and buckling mode of the RA-WCTH when folded to 45° for different optimization designs. For clarity, only the middle section of the structure is shown. The results indicate that the material failure risk is mainly concentrated at the edges of the cutouts, but after optimization, the failure indices for all designs are reduced below the safety threshold. Moreover, the multi-objective optimized design also has the highest critical buckling load. The optimal cutout design obtained using the Level-Set method proposed by Ferraro[46] is used as the benchmark for validating the effectiveness of the proposed method in this study. The black dashed line in Fig. 10 (b) represents the quasi-static bending experimental test results of the optimal design obtained by Level-Set, while the red curve shows the simulation results computed using the finite element model established in this study. The two closely match, proving the reliability of the numerical model and optimization results. The right side of Fig. 10 (c) shows the optimal cutout layout obtained by Level-Set, along with the corresponding bending stiffness, critical buckling load, and stored strain energy.

Under the failure constraint, the optimized design (Fig. 10 (a)) enhances both bending stiffness and critical buckling load by 107.75% and 420.47%, respectively. Regardless of whether considering the single-objective optimization results (Fig. 6), the bi-objective optimization results (Fig. 7 and Fig. 8), or the multi-objective optimization results (Fig. 10), the stored strain energy of the RA-WCTH consistently exhibits a positive correlation with bending stiffness. Furthermore, the optimal design also results in a notable 34.05% increase in this energy metric.

The minimum strip width of the Level-Set optimized results is 1 mm. In preliminary studies on scale effect verification, it was found that considering the actual strength parameters shown in Table 6 does not affect the macroscopic structural response (Fig. 10(b)). However, significant differences were observed in the failure assessments. After accounting for scale effects, the maximum failure index of RA-WCTH increased from 0.839 to 2.664. Damage appeared in a 0.2 mm2 area within the narrow strip of RA-WCTH, which occupies a very small portion of the strip's total area. Based on X-ray CT scans combined with RA-WCTH bending tests, this minimal damage does not compromise the structural integrity or macroscopic performance. In contrast, the optimal design obtained in this study (Fig. 10(a)) has a minimum strip width of 2.34 mm, which is more than twice the Level-Set result (2.34 mm vs. 1 mm). This increase further mitigates scale effects, thereby enhancing the reliability of the optimization results.

5. Conclusion

Foldable, storable, and self-deployable thin-walled composite shell structures with cutouts have enormous potential in deployable structures. It is well-established that the position, number, and shape of cutouts have a significant impact on the folding, deployment, and load-bearing performance of these structures. Achieving comprehensive consideration of these design elements while optimizing multiple performance metrics poses a significant challenge to both dimensional and shape optimization. The topology optimization method based on element density design variables offers a new approach to reshaping the void-solid regions of structures from the perspective of material re-distribution, providing new inspiration for the cutout design of deployable thin-walled composite shell structures. However, existing topology optimization models struggle to directly address the complex anisotropy, failure constraints, and buckling stability of woven composites, making this a relatively unexplored topic in deployable composite thin-walled shell structures.

The explicit contribution of this study is the development of a multi-objective topology optimization method specifically designed for DCTWS cutouts design. This method aims to maximize the bending stiffness, stored strain energy, and critical buckling load of the structure while satisfying the failure constraints of woven composite materials—something that current specialized topology optimization tools or integrated modules in commercial software cannot achieve. Starting from the elastic constitutive model of the ABD matrix for woven composite laminates, explicit sensitivity expressions for structural stiffness (compliance), critical buckling load, and the modified Tsai-Wu failure criterion are derived. These expressions were then linearly aggregated to construct a multi-objective topology optimization model capable of switching across various optimization problems. This model was applied to the cutout design of a complex DCTWS structure, specifically the RA-WCTH. The impact of weight factors on cutout design and optimization objectives is thoroughly discussed. By exploring a wide range of weighting schemes, a Pareto front for RA-WCTH is constructed and six representative cutout designs are clustered. A comparison with the optimization design and experimental results from existing literature on RA-WCTH demonstrated that the proposed method offers a broader design space and superior optimization performance, thereby validating the correctness and advantages of the topology optimization model presented in this study.

More importantly, this topology optimization theory was successfully integrated with commercial finite element software ABAQUS via Python scripts, enabling flexible switching between optimization problems and extending its application to lightweight or cutout optimization of various DCTWS. This work not only expands the theoretical framework of topology optimization for anisotropic thin-shell structures but also contributes to advancing the integration of topology optimization theory with engineering software.

The limitations of the proposed method and future directions for improvement are outlined. Firstly, it has been preliminarily applied to RA-WCTH structures with a small folding angle (45 deg). Extending it to other DCTWS structures, such as high-strain deployable systems with a 180 deg folding angle,[10,13] may face convergence challenges. Secondly, in deriving the sensitivity for the failure index, the adjoint vector was omitted. Enhancing numerical stability and developing a sensitivity model that incorporates the adjoint vector for anisotropic shell failure criteria are critical future steps. Additionally, while the linear weighted aggregation method is widely used in multi-objective topology optimization, constructing a

well-distributed Pareto front requires exploring many weight combinations, leading to high computational costs and reduced efficiency. Future research will focus on three areas: (1) integrating configuration-based clustering to develop adaptive weighting strategies for improved diversity and efficiency,[58] (2) combining sampling methods with machine learning to create surrogate models for faster Pareto front prediction and (3) developing advanced algorithms, such as IGA and MMC,[59,60] tailored for anisotropic shell elements to reduce design variables and produce structures with clear boundaries. These improvements will expand the applicability of topology optimization to a wider range of DCTWS structures.

CRediT authorship contribution statement

Hao JIN: Writing – review & editing, Writing – original draft. **Ning AN:** Writing – review & editing. **Qilong JIA:** Funding acquisition. **Chun SHAO:** Funding acquisition. **Xiaofei MA:** Supervision. **Jinxiong ZHOU:** Supervision.

Declaration of competing interest

The authors declare that they have no known competing financial interests or personal relationships that could have appeared to influence the work reported in this paper.

Acknowledgements

This research was supported by the National Natural Science Foundation of China(No. 12202295), the International (Regional) Cooperation and Exchange Projects of the National Natural Science Foundation of China (No. W2421002), the Sichuan Science and Technology Program (No. 2025ZNSFSC0845), Zhejiang Provincial Natural Science Foundation of China (No. ZCLZ24A0201) and the Fundamental Research Funds for the Provincial Universities of Zhejiang (No. GK249909299001-004).

References

1. Ma XF, An N, Cong Q, et al. Design, modeling, and manufacturing of high strain composites for space deployable structures. *Commun Eng* 2024;**3**(78):1–18.
2. Mobrem M, Adams DS. Deployment analysis of the lenticular jointed antennas onboard the mars express spacecraft. *J Spacecr Rockets* 2009;**46**(2):394–402.
3. Fischer G, Panchenko M, Macher W, et al. Calibration of the JUICE RWI antennas by numerical simulation. *Radio Sci* 2021;**56**(11):1–23.
4. Lopatin AV, Morozov EV, Kazantsev ZA, et al. Deployment analysis of a composite thin-walled toroidal rim with elastic hinges: application to an umbrella-type reflector of spacecraft antenna. *Compos Struct* 2023;**306**:116566.
5. Footdale JN, Banik JA, Murphey TW. Design developments of a non-planar deployable structure. *51st AIAA/ASME/ASCE/AHS/ASC structures structural dynamics, and materials conference, 18th AIAA/ASME/AHS adaptive structures conference*, 2010. p. 2608.
6. Footdale JN, Banik JA. System design study of a deployable reflector antenna with flexible shell segments. *3rd AIAA spacecraft structures conference*, 2016. p. 0698.
7. Ferraro S, Pellegrino S. Self-deployable joints for ultra-light space structures. *2018 AIAA spacecraft structures conference*, 2018. p. 0694.
8. Tan LT, Pellegrino S. Thin-shell deployable reflectors with collapsible stiffeners Part 1: approach. *AIAA J* 2006;**44**(11):2515–23.
9. Okuizumi N, Watanabe A, Ito H. Efficient storage and deployment of tubular composite boom using spring root hinges. *J Spacecr Rockets* 2021;**58**(2):334–44.
10. Palmeri F, Laurenzi S, Pellegrino S. *Root boundary conditions for omega deployable booms. AIAA SCITECH 2024 forum*, 2024. p. 0849.
11. Mallikarachchi HM. Thin-walled composite deployable booms with tape-spring hinges [dissertation]. Cambridge: University of Cambridge; 2011.
12. Jin H, An N, Jia QL, et al. Optimizing deployment dynamics of composite tape-spring hinges. *Thin Walled Struct* 2024;**198**:111738.
13. Jin H, Jia QL, An N, et al. Surrogate modeling accelerated shape optimization of deployable composite tape-spring hinges. *AIAA J* 2022;**60**(10):5942–53.
14. Fernandes P, Pinto R, Ferrer A, et al. Performance analysis of a damage tolerant composite self-deployable elastic-hinge. *Compos Struct* 2022;**288**:115407.
15. Kunakorn-ong P, Santer M. Optimal design of tube flexure cut-out geometries for viscoelastic resilience and deployment performance. *Acta Astronaut* 2024;**216**:282–94.
16. Liu TW, Bai JB, Fantuzzi N, et al. Multi-objective optimisation designs for thin-walled deployable composite hinges using surrogate models and Genetic Algorithms. *Compos Struct* 2022;**280**:114757.
17. Yang H, Liu RQ, Wang Y, et al. Experiment and multiobjective optimization design of tape-spring hinges. *Struct Multidiscip Optim* 2015;**51**:1373–84.
18. Gao J, Xiao M, Zhang Y, et al. A comprehensive review of isogeometric topology optimization: methods, applications and prospects. *Chin J Mech Eng* 2020;**33**:1–14.
19. Bendsøe MP, Sigmund O. *Topology optimization: theory, methods, and applications*. Berlin: Springer Science & Business Media; 2013.
20. Xia L, Xia Q, Huang XD, et al. Bi-directional evolutionary structural optimization on advanced structures and materials: a comprehensive review. *Arch Comput Methods Eng* 2018;**25**:437–78.
21. Sui YK, Peng XR. *Modeling, solving and application for topology optimization of continuum structures: ICM method based on step function*. Oxford: Butterworth-Heinemann; 2017.
22. Van Dijk NP, Maute K, Langelaar M, et al. Level-set methods for structural topology optimization: a review. *Struct Multidiscip Optim* 2013;**48**(3):437–72.
23. Guo X, Zhang WS, Zhang J, et al. Explicit structural topology optimization based on moving morphable components (MMC) with curved skeletons. *Comput Methods Appl Mech Eng* 2016;**310**:711–48.
24. Xu YJ, Zhu JH, Wu Z, et al. A review on the design of laminated composite structures: constant and variable stiffness design and topology optimization. *Adv Compos Hybrid Mater* 2018;**1**:460–77.
25. Nikbakt S, Kamarian S, Shakeri M. A review on optimization of composite structures Part I: laminated composites. *Compos Struct* 2018;**195**:158–85.
26. Zhou H, Zhu JH, Wang C, et al. Optimization design for 3D-braided composite structure under thermo-mechanical load. *Struct Multidiscip Optim* 2023;**66**(8):193.
27. Ma ZD, Kikuchi N, Pierre C, et al. Multidomain topology optimization for structural and material designs. *J Appl Mech* 2006;**73**(4):565–73.

28. Stegmann J, Lund E. Discrete material optimization of general composite shell structures. *Int J Numer Methods Eng* 2005;**62**(14):2009–27.
29. Duan ZY, Liu YQ, Fan JL, et al. Concurrent multi-material and multi-scale design optimization of fiber-reinforced composite material and structures for minimum structural compliance. *Compos Struct* 2023;**311**:116796.
30. Boddeti N, Tang YL, Maute K, et al. Optimal design and manufacture of variable stiffness laminated continuous fiber reinforced composites. *Sci Rep* 2020;**10**(1):16507.
31. Li SY, Hou SJ. Two-scale concurrent optimization of composites with elliptical inclusions under microstress constraints within the FE2 framework. *Comput Struct* 2023;**276**:106942.
32. Zhao A, Li P, Cui YH, et al. Multiscale topology optimization with Direct FE2. *Comput Methods Appl Mech Eng* 2024;**419**:116662.
33. Jensen PDL, Sigmund O, Groen JP. De-homogenization of optimal 2D topologies for multiple loading cases. *Comput Methods Appl Mech Eng* 2022;**399**:115426.
34. Lee JW, Kim JJ, Yoon GH. Stress constraint topology optimization using layerwise theory for composite laminates. *Compos Struct* 2019;**226**:111184.
35. Zhang XB, Zhou YY, Xia L, et al. Evolutionary topology optimization with stress control for composite laminates using Tsai-Wu criterion. *Comput Methods Appl Mech Eng* 2025;**434**:117570.
36. Yee JCH, Pellegrino S. Composite tube hinges. *J Aerosp Eng* 2005;**18**(4):224–31.
37. Xu T, Huang XD, Lin XS, et al. Topology optimization for maximizing buckling strength using a linear material model. *Comput Methods Appl Mech Eng* 2023;**417**:116437.
38. Neves MM, Rodrigues H, Guedes JM. Generalized topology design of structures with a buckling load criterion. *Struct Multidiscip Optim* 1995;**10**:71–8.
39. Ferrari F, Sigmund O. A strategy for avoiding spurious localized buckling modes in topology optimization. *Int J Numer Methods Eng* 2023;**124**(18):4118–40.
40. Ferraro S, Pellegrino S. Topology and shape optimization of ultrathin composite self-deployable shell structures with cutouts. *AIAA J* 2021;**59**(9):3696–709.
41. Fernandes P, Pinto R, Correia N. Design and optimization of self-deployable damage tolerant composite structures: a review. *Compos Part B-Eng* 2021;**221**:109029.
42. Soykasap Ö. Micromechanical models for bending behavior of woven composites. *J Spacecr Rockets* 2006;**43**(5):1093–100.
43. Zuo ZH, Xie YM. A simple and compact Python code for complex 3D topology optimization. *Adv Eng Software* 2015;**85**:1–11.
44. Mallikarachchi H, Pellegrino S. Failure criterion for two-ply plain-weave CFRP laminates. *J Compos Mater* 2013;**47**(11):1357–75.
45. Munk DJ, Vio GA, Steven GP. A simple alternative formulation for structural optimisation with dynamic and buckling objectives. *Struct Multidiscip Optim* 2017;**55**:969–86.
46. Ferraro S. Topology optimization and failure analysis of deployable thin shells with cutouts [dissertation]. California: California Institute of Technology; 2020.
47. Ferraro S, Pellegrino S. Size effects in plain-weave Astroquartz® deployable thin shells. *J Compos Mater* 2021;**55**(18):2417–30.
48. An N, Jia QL, Jin H, et al. Multiscale modeling of viscoelastic behavior of unidirectional composite laminates and deployable structures. *Mater Des* 2022;**219**:110754.
49. Jin H, An N, Jia QL, et al. A mesoscale computational approach to predict ABD matrix of thin woven composites. *Compos Struct* 2024;**337**:118031.
50. Teimouri M, Asgari M. Multi-objective BESO topology optimization for stiffness and frequency of continuum structures. *Struct Eng Mech* 2019;**72**(2):181–90.
51. Zhao Z, Zhang XS. Encoding reprogrammable properties into magneto-mechanical materials via topology optimization. *NPJ Comput Mater* 2023;**9**(1):57.
52. Huang XD, Xie YM. *Evolutionary topology optimization of continuum structures: methods and applications*. Hoboken: John Wiley & Sons; 2010.
53. Nabaki K, Shen JH, Huang XD. Stress minimization of structures based on bidirectional evolutionary procedure. *J Struct Eng* 2019;**145**(2):04018256.
54. Deng H, Vulimiri PS, To AC. An efficient 146-line 3D sensitivity analysis code of stress-based topology optimization written in MATLAB. *Optim Eng* 2023;**23**:1733–57.
55. Kambampati S, Gray JS, Kim HA. Level set topology optimization of structures under stress and temperature constraints. *Comput Struct* 2020;**235**:106265.
56. Fernandes P, Ferrer À, Gonçalves P, et al. Stress-constrained topology optimization for commercial software: a python implementation for abaqus®. *Appl Sci* 2023;**13**(23):12916.
57. Cheikh M, Jarboui B, Loukil T, et al. A method for selecting Pareto optimal solutions in multiobjective optimization. *J Inform Math Sci* 2010;**2**(1):51–62.
58. Ryu N, Seo M, Min S. Multi-objective topology optimization incorporating an adaptive weighed-sum method and a configuration-based clustering scheme. *Comput Methods Appl Mech Eng* 2021;**385**:114015.
59. Gao J, Chen C, Fang XB, et al. Multi-objective topology optimization for solid-porous infill designs in regions-divided structures using multi-patch isogeometric analysis. *Comput Methods Appl Mech Eng* 2024;**428**:117095.
60. Liu C, Zhu YC, Sun Z, et al. An efficient moving morphable component (MMC)-based approach for multi-resolution topology optimization. *Struct Multidiscip Optim* 2018;**58**:2455–79.